ANCF curvature continuity: Application to soft and fluid materials

Ahmed A. Shabana* (shabana@uic.edu)
Dayu Zhang (dayu33@uic.edu)

Department of Mechanical and Industrial Engineering
University of Illinois at Chicago
842 West Taylor Street
Chicago, IL 60607

* Corresponding author

Abstract

The continuity of the position-vector gradients at the nodal points of a finite element (FE) mesh does not always ensure the continuity of the gradients at the element interfaces. Discontinuity of the gradients at the interface not only adversely affects the quality of the simulation results, but can also lead to computer models that do not properly represent realistic physical system behaviors, particularly in the case of soft and fluid material applications. In this study, the *absolute nodal coordinate formulation* (ANCF) finite elements are used to define general *curvature-continuity* conditions that allow for eliminating or minimizing the discontinuity of the position gradients at the element interface. For the ANCF solid element, with four-node surfaces, it is shown that continuity of the gradients tangent to an arbitrary point on a surface is ensured as the result of the continuity of the gradients at the nodal points. The general ANCF continuity conditions are applicable to both reference-configuration straight and curved geometries. These conditions are formulated without the need for using the computer-aided-design (CAD) knot vector and knot multiplicity, which do not account properly for the concept of system degrees of freedom. The ANCF curvature-continuity conditions are written in terms of constant geometric coefficients obtained using the matrix of position-vector gradients that defines the reference-configuration geometry. The formulation of these conditions is demonstrated using the ANCF fully-parametrized three-dimensional solid and tetrahedral elements, which employ a complete set of position gradients as nodal coordinates. Numerical results are presented in order to examine the effect of applying the curvature-continuity conditions on achieving a higher degree of smoothness at the element interfaces in the case of soft and fluid materials.

Keywords: Curvature continuity; position gradients; absolute nodal coordinate formulation; soft and fluid materials; integration of geometry and analysis.

1. Introduction

Finite elements (FE) based on the absolute nodal coordinate formulation (ANCF), which have been used in the analysis of large-deformation problems, can describe arbitrarily large motion because of the use of position gradients as nodal coordinates [1 – 11]. For accurate formulation of the equations of motion that govern the dynamics of flexible bodies, a distinction is made between position and displacement gradients. Position gradients are tangent to coordinate lines (fibers), while displacement gradients do not have this important geometric interpretation [12]. This important geometric property of the position gradients allowed over the past few years introducing new concepts and FE formulations that can contribute successful integration of the geometry and analysis and for addressing many of the computer-aided-engineering (CAE) challenges that cannot be addressed using existing FE technology [13 - 18].

The standard FE assembly of ANCF finite elements ensures the continuity of the position gradients at the nodal points. This, in turn, ensures the continuity of the rotation, strain, and stress fields at the FE mesh nodal points. Nonetheless, the continuity of the position gradients at the nodes of an FE mesh does not ensure the continuity of these gradients at the element interfaces. Such a gradient discontinuity at the element interface not only has an adverse effect on the quality of the simulation results in some important applications, but can also lead to computer models that do not properly describe the system behavior, particularly in the case of soft and fluid materials. For example, in the case of fluids, the constitutive equations are formulated in terms of the time rate of the position gradients using the Navier-Stokes equations [19]. Discontinuity of the gradients at the element interfaces can lead to discontinuities in the viscous stresses and the resulting fluid damping forces. Similarly, in the case of soft materials which can experience large deformations, the gradient discontinuity at the element interface can lead to discontinuity of the rotation, strain, and stress fields that can have adverse effect on the accuracy of the computer models.

The use of the position gradients as nodal coordinates allows for conveniently shaping the element geometry. If the position gradients are not used as nodal coordinates, regardless of whether or not they can be computed at arbitrary points, describing the element geometry in the reference configuration can be difficult even when conventional isoparametric elements are used. As demonstrated in this study, the matrix of position-vector gradients that defines the reference-configuration geometry enters into the definitions of the general curvature equations that are applicable to both straight and curved geometries. Therefore, it is not straightforward to formulate these general curvature equations using conventional finite elements or rotation-based elements that do not employ position gradients as nodal coordinates [13 - 18]. The position gradients do not only enter in the formulations of the strains and stresses, but also define the stress-free reference configuration. Consequently, their use as nodal coordinates is necessary in order to be able to develop realistic and geometrically-accurate models without the need for using the B-spline (Basis Splines) and NURBS (Non-Uniform Rational B-Splines) control points, knot multiplicity, and knot vectors [20 - 22]. B-splines and NURBS were developed as graphics tools without consideration of the important concept of the degrees of freedom which is fundamental in mechanics. Therefore, such graphics tool can have limited potential in addressing the fundamental and challenging CAE problems, and their use in analysis will put severe restrictions on the types of models that can be developed in the future. In fact, the appropriateness of using B-spline and NURBS representations in developing physics-based models for visualization and computer animations has been debated by the computer science research communities for decades [23 - 28].

In this study, ANCF finite elements are used to formulate *curvature-continuity* conditions that allow for eliminating or minimizing the discontinuity of the position gradients at the element interface. The general ANCF continuity conditions developed in this investigation are applicable to both straight and curved reference-configuration geometries, and as previously mentioned, do not require the use of the CAD control points, knot vectors, and knot multiplicity which do not properly account for the concept of degrees of freedom. In order to properly account for the stress-free reference-configuration geometry, the ANCF curvature-continuity conditions are formulated in terms of constant *geometric coefficients* obtained using the elements of the matrix of position-vector gradients that defines the mapping between the straight and curved reference-configuration geometries. The formulation of these conditions is demonstrated using the three-dimensional ANCF fully-parametrized eight-node solid and four-node tetrahedral elements; each of which has twelve coordinates per node; three position and nine gradient coordinates [6, 29, 30]. One of the basic differences between the ANCF solid and tetrahedral elements used in this paper is the type of parameterization and gradients used. For the ANCF fully-parametrized tetrahedral element, two different position gradients are introduced; the volume and Cartesian gradients. The volume gradients are systematically converted to Cartesian gradients in order to allow using a standard FE assembly procedure. For the fully-parametrized ANCF solid element, on the other hand, only Cartesian gradients are used. Using the ANCF solid and tetrahedral elements, numerical results are obtained in order to demonstrate the effect of applying the curvature-continuity conditions on reducing the element-interface gradient discontinuities in the case of soft and fluid materials.

2. Problem definition

Enforcing higher degree of continuity at the nodal points of an FE mesh can contribute to achieving higher degree of smoothness at the element interface. In general, continuity of the position gradients at the nodal points does not ensure continuity of the same gradients at the element interface. One option to achieve a higher degree of smoothness at the element interface is to impose curvature-continuity conditions at the nodal points. Achieving a higher degree of smoothness at the element interface is particularly important in the case of soft and fluid materials in which the definition of the forces, including the viscous forces, depends on the position gradients and their time rate. Figures 1 shows the ANCF solid and tetrahedral elements considered in this study to examine the effect of enforcing the curvature continuity [6, 29, 30]. The ANCF solid element has 8 nodes, while the ANCF tetrahedral element has 4 nodes. Each node of these two elements has twelve nodal coordinates that include three position and nine gradient coordinates. The shape functions of the two elements are provided in Appendix A of this paper. The displacement field of these two elements is written as $\mathbf{r}(\mathbf{x},t)=\mathbf{S}(\mathbf{x})\mathbf{e}(t)$, where $\mathbf{r}$ is the global position vector, $\mathbf{S}$ is the element shape function matrix, $\mathbf{e}$ is the vector of nodal coordinates, t is time, and $\mathbf{x}=\begin{bmatrix}x_1 & x_2 & x_3\end{bmatrix}^T$ is the vector of the element spatial coordinates. The vector of the coordinates at a node k of the ANCF solid and tetrahedral elements can be written as $\mathbf{e}^k=\begin{bmatrix}\mathbf{r}^{k^T} & \mathbf{r}_{x_1}^{k^T} & \mathbf{r}_{x_2}^{k^T} & \mathbf{r}_{x_3}^{k^T}\end{bmatrix}^T$, where superscript k refers to the node number, and $\mathbf{r}_{x_j}=\partial\mathbf{r}/\partial x_j$, $j=1,2,3$, are the position gradient vectors.

2.1 Illustrative example

Figure 2 shows a flexible pendulum made of soft material that is connected to rigid body at points O_1, O_2, O_3, and O_4 by four spherical joints. The pendulum is modeled using simple ANCF solid- and tetrahedral-element meshes. In this example, the rigid body is connected to the ground by a revolute joint that allows for only relative rotation about the X_2 axis. The coordinate system $X_1X_2X_3$ is selected as the structure coordinate system, which is initially parallel to the global coordinate system. The dimensions of the two meshes are $a = 1\ \text{m}, b = c = 0.2\ \text{m}$, and the numbers of the elements in the solid-element and tetrahedral-element meshes are assumed two and five, respectively. This simple example, which is used in this section to demonstrate the position-gradient discontinuity at the element interface, will be further examined in the numerical results section where the model material properties and other mesh dimensions are presented and discussed in more detail. The standard assembly of the ANCF meshes ensures the continuity of the position gradients at the nodes. In order to examine the continuity of the gradients at the element interface, the rigid body is allowed to rotate about the X_2 axis freely from an initial horizontal configuration. The motion about this axis is assumed to be specified and defined by the function $\varphi(t)=2\omega t$, where ω is a constant angular velocity that equal to $1\,\text{rad/s}$. The effect of gravity is neglected in this example.

In order to use this simple example to demonstrate the fact that the continuity of the position gradients at the nodes does not guarantee the same continuity at an arbitrary point on the element interface, the central point B on the element interface shown in Fig. 2 is considered. The standard ANCF FE assembly process ensures continuity of both position and gradient coordinates at the nodal points when two elements are rigidly connected. For the solid-element mesh, the position-gradient continuities $\left(C^1\right)_{x_2}$ and $\left(C^1\right)_{x_3}$ at the element interface are automatically achieved as the result of the standard FE assembly, while the $\left(C^1\right)_{x_1}$ position-gradient continuity is not ensured, where the notation $\left(C^l\right)_{\alpha}$ implies lth degree of continuity ($l=0$ for position, and $l=1$ for position gradients) associated with the coordinate $\alpha = x_1, x_2, x_3$.When assembling solid elements, the connectivity interface defines a surface whose geometry is described by two parameters. The continuity of the two gradients associated with these two parameters at the element interface surface is ensured as the result of the continuity of the gradients at the nodal points, as will be explained in the following sub-section. On the other hand, the continuity of the third gradient associated with the remaining coordinate at the element interface surface is not ensured. Figure 3 shows the difference in the first element of the gradient vectors $\Delta\mathbf{r}_{x_1}$ at point B when it is evaluated using the two neighboring finite elements that share this point. This difference can be used as a measure of the degree of the position-gradient discontinuity at the element interface. It is clear from the results presented in this figure that the position gradients are not continuous for the soft material example considered. Figure 4 shows the differences in the results as measured by $\Delta\mathbf{r}_{x_j}(j), j = 1,2,3$ at point B when the tetrahedral-element mesh is used. The results presented in this figure also show the discontinuities in the position gradients at the element interface. Similar position-gradient discontinuities at the element interface are also observed with the components of other gradient vectors. Furthermore, numerical studies performed in this investigation demonstrated that conventional lower-order tetrahedral finite elements which enforce only position continuity at the nodal points suffer from more serious gradient discontinuity problems at the element interface. The displacement field of the conventional tetrahedral element used in these numerical studies is presented in the appendix of this paper.

2.2 Discussion of the results

The results obtained in the example discussed in this section demonstrate that the position-gradient vectors associated with the parameters x_2 and x_3 of the element interface surface are continuous everywhere on such an interface surface as the result of imposing the ANCF position-gradient continuity at the nodal points. On the other hand, the position-gradient vector associated with the third parameter x_1 is not continuous on the interface surface despite the continuity of this gradient vector at the nodal points. This interesting result can be explained by recognizing the fact that for a given value for the coordinate x_1, the interface surface is defined by a two-parameter polynomial which has twelve coordinates as shown in the appendix of the paper. For a given value of the coordinate x_1, this cubic interpolating polynomial is function of the two parameters x_2 and x_3 only. Therefore, imposing the continuity on $\mathbf{r}, \mathbf{r}_{x_2}$, and $\mathbf{r}_{x_3}$ at the nodal points leads to twelve conditions that ensure that the two surfaces on the two elements are identical. This position-gradient continuity can be achieved at the cubic element-interface surface because the solid element surface has four nodes that can be used to define the twelve constraint equations that ensure that the two surfaces on the two elements are the same. These twelve conditions cannot be obtained for the four-node tetrahedral element which has interface surfaces defined by three nodes only, and therefore, there are only nine conditions available when imposing the continuity of $\mathbf{r}, \mathbf{r}_{x_2}$, and $\mathbf{r}_{x_3}$ at the nodal points. The tetrahedral-element nine conditions are not sufficient to ensure that the two interface cubic surfaces of the two elements have the same geometry, and therefore, there is no guarantee that these two interface surfaces are the same. This explains the $\mathbf{r}_{x_2}$, and $\mathbf{r}_{x_3}$ discontinuity results obtained using the simple example discussed in this section in the case of the tetrahedral element. For any surface on the tetrahedral element, one can always define two gradient vectors tangent to a tetrahedral surface and a third gradient vector normal to the surface by using gradient tensor transformation. The gradient vector normal to the surface does not enter into the surface definition, and therefore, the continuity of the position and the two gradient vectors tangent to the surface only contribute to the definition of the cubic surface.

Based on the discussion presented in this section, any ANCF element (solid or plate), which can be used to define four-node surfaces ensures that there will be no gaps at the element interfaces. This is an important feature that can be effectively exploited for developing new composite-structure models which can be developed using conventional finite elements. The ANCF continuity conditions at the nodal points ensure that the two interface surfaces of two elements have the same geometry and location, and therefore, there are no gaps at the element interfaces. Accomplishing such an important geometric feature is not even straight forward when B-splines and NURBS, which employ control points, are used. Furthermore, as discussed in this paper, the matrix of the position-vector gradients in the reference configuration plays a fundamental role in the definition of the continuity conditions.

2.3 Proposed solution

A higher degree of smoothness can be achieved by imposing higher degree of continuity at the nodal points. For example, curvature continuity at the nodal points can be used to achieve a higher degree of smoothness at the element interface. Imposing the curvature continuity has also the advantage of reducing the model dimensions. Curvature-continuity conditions can be systematically formulated and applied at a preprocessing stage. Dependent mesh variables can be eliminated, leading to a reduced-order model. Having such a capability of adjusting the degree of continuity is necessary for the integration of geometry and analysis and for the development of future mechanics-based CAD systems. Using the mechanics-based approach described in this investigation, position, gradient, and curvature continuities can be enforced independently, a feature that is necessary for efficient formulation of the MBS joint constraint equations using ANCF finite elements.

2.4 CAD/analysis systems

By adopting the mechanics-based approach described in this section to adjust the degree of continuity, the use of the knot multiplicity and knot vectors of B-splines and NURBS can be avoided, while properly accounting for the correct number of degrees of freedom of the system. While determining the correct number of degrees of freedom as the result of properly imposing any algebraic constraint conditions is a major mechanics issue that cannot be ignored, there is another major limitation of using the graphics-based B-spline and NURBS representations as analysis tools [31]. When the B-spline and NURBS knot multiplicity and knot vectors are used, gradient continuity cannot be enforced before enforcing position continuity, and curvature continuity cannot be enforced before imposing both position and gradient continuities. This serious drawback limits the scope of future CAD/analysis systems by excluding some of the constraints or joints which can be formulated as linear algebraic equations at a preprocessing stage. For example, the formulation of linear ANCF joint constraints may require imposing conditions on the gradient vectors in some directions without imposing position constraints in the same directions. Because ANCF meshes do not require the use of local frames as it is the case with the *floating frame of reference* (FFR) formulation, two gradient vectors at two points on two ANCF finite elements i and j along a certain fiber defined by the parameter β can be assumed equal using the linear algebraic equations $\partial \mathbf{r}^i / \partial \beta = \partial \mathbf{r}^j / \partial \beta$, where the superscript refers to the element number in the mesh. A large number of algebraic constraint equations, traditionally formulated as highly nonlinear equations in the MBS literature, can be formulated as linear equations using ANCF finite elements; thereby allowing for the elimination of a large number of dependent variables at a preprocessing stage, as previously discussed and also demonstrated in the literature.

The curvature-continuity conditions derived in this investigation shed light on the importance of using the position gradients as nodal coordinates and also explain some of the fundamental problems that will be encountered if B-splines and NURBS are used to obtain these equations. In the case of stress-free initially curved geometry, the matrix of position-vector gradients must be formulated and used in the computations of the strains and stresses in a manner consistent with the theory of continuum mechanics. As will be clear from the analysis presented in this investigation, properly formulating some of the algebraic equations for curved reference-configuration geometry does not preserve the B-spline and NURBS rigid recurrence structure. Therefore, such a rigid recurrence structure will be eventually destroyed if general CAD/analysis algorithms are to be developed in the future. This because curvature continuity conditions, as demonstrated in this paper, require the use of the matrix of position-vector gradients in the reference stress-free configuration. This matrix cannot be accounted for using the B-spline and NURBS knot multiplicity and knot vector. Furthermore, such B-splines and NURBS approach for increasing the degree of continuity does not always lead to the correct number of degrees of freedom Consequently, general continuity conditions cannot, in general, be handled by B-splines and NURBS without destroying their rigid recurrence structure [34].

3. General curvature definitions

In order to define the general curvature equations in the case of of initially curved reference configuration, the straight-element and curved-structure coordinates (parameters) are defined, respectively, as

$$\mathbf{x} = \begin{bmatrix} x_1 & x_2 & x_3 \end{bmatrix}^T, \qquad \mathbf{X} = \begin{bmatrix} X_1 & X_2 & X_3 \end{bmatrix}^T \tag{1}$$

The use of the structure coordinates $\mathbf{X}$ is necessary in order to be able to properly impose the constraint equations between two different finite elements. The matrices of position-vector gradients defined with respect to the element and structure coordinates are defined, respectively, as

$$\mathbf{J}_e = \begin{bmatrix} \mathbf{r}_{x_1} & \mathbf{r}_{x_2} & \mathbf{r}_{x_3} \end{bmatrix}, \qquad \mathbf{J} = \begin{bmatrix} \mathbf{r}_{X_1} & \mathbf{r}_{X_2} & \mathbf{r}_{X_3} \end{bmatrix} \tag{2}$$

where $\mathbf{r}_\alpha = \partial \mathbf{r} / \partial \alpha$. One also has

$$\mathbf{J} = \mathbf{J}_e \mathbf{J}_o^{-1} \tag{3}$$

where, when using the ANCF kinematic description, $\mathbf{J}_o = \mathbf{S}\mathbf{e}_o$ is the matrix of the position-vector gradients that accounts for the stress-free reference configuration. This matrix is the identity matrix if the reference configuration is not curved. Because, in the case of general geometry, $\mathbf{J}_o \mathbf{J}_o^{-1} = \mathbf{I}$, where $\mathbf{I}$ is the 3×3 identity matrix, one has

$$\left(\mathbf{J}_o\right)_{x_k} \mathbf{J}_o^{-1} + \mathbf{J}_o \left(\mathbf{J}_o^{-1}\right)_{x_k} = \mathbf{0}, \qquad k = 1,2,3 \tag{4}$$

This equation leads to the following identity

$$\left(\mathbf{J}_o^{-1}\right)_{x_k} = -\mathbf{J}_o^{-1} \left(\mathbf{J}_o\right)_{x_k} \mathbf{J}_o^{-1}, \qquad k = 1,2,3 \tag{5}$$

In this equation, $\left(\mathbf{J}_o\right)_{x_k} = \partial \mathbf{J}_o / \partial x_k$. The identity of Eq. 5 enables computing the derivatives of the inverse of $\mathbf{J}_o$ from the derivative of $\mathbf{J}_o$. Therefore, upon using this identity, one can write

$$\left(\mathbf{J}\right)_{X_j} = \left(\mathbf{J}_e \mathbf{J}_o^{-1}\right)_{X_j} = \begin{bmatrix} \mathbf{r}_{X_1 X_j} & \mathbf{r}_{X_2 X_j} & \mathbf{r}_{X_3 X_j} \end{bmatrix}, \qquad j = 1,2,3 \tag{6}$$

This equation, in which $\left(\mathbf{J}\right)_{X_j} = \partial \mathbf{J} / \partial X_j$ and $\left(\mathbf{J}_e \mathbf{J}_o^{-1}\right)_{X_j} = \partial \mathbf{J}_e \mathbf{J}_o^{-1} / \partial X_j$, can be written as

$$\left(\mathbf{J}\right)_{X_j} = \begin{bmatrix} \mathbf{r}_{X_1 X_j} & \mathbf{r}_{X_2 X_j} & \mathbf{r}_{X_3 X_j} \end{bmatrix} = \sum_{k=1}^{3} \left(\mathbf{J}_e \mathbf{J}_o^{-1}\right)_{x_k} \frac{\partial x_k}{\partial X_j} = \sum_{k=1}^{3} \left(\mathbf{J}_e \mathbf{J}_o^{-1}\right)_{x_k} \alpha_{kj} \qquad j = 1,2,3 \tag{7}$$

where $\alpha_{kj} = \partial x_k / \partial X_j$, $j,k = 1,2,3$. Therefore, the matrix $\mathbf{J}_o^{-1}$ can be written as

$$\mathbf{J}_o^{-1} = \begin{bmatrix} \mathbf{C}_{J1} & \mathbf{C}_{J2} & \mathbf{C}_{J3} \end{bmatrix}$$
$$= \begin{bmatrix} \partial x_1/\partial X_1 & \partial x_1/\partial X_2 & \partial x_1/\partial X_3 \\ \partial x_2/\partial X_1 & \partial x_2/\partial X_2 & \partial x_2/\partial X_3 \\ \partial x_3/\partial X_1 & \partial x_3/\partial X_2 & \partial x_3/\partial X_3 \end{bmatrix} = \begin{bmatrix} \alpha_{11} & \alpha_{12} & \alpha_{13} \\ \alpha_{21} & \alpha_{22} & \alpha_{23} \\ \alpha_{31} & \alpha_{32} & \alpha_{33} \end{bmatrix}. \tag{8}$$

where $\mathbf{C}_{Jj}$ is the jth column of $\mathbf{J}_o^{-1}$, that is, $\alpha_{kl} = \partial x_k/\partial X_l,\, k,l = 1,2,3$. Using this definition, one can write the general expression for the curvatures as

$$\begin{aligned} \begin{bmatrix} \mathbf{r}_{X_1X_j} & \mathbf{r}_{X_2X_j} & \mathbf{r}_{X_3X_j} \end{bmatrix} &= \sum_{k=1}^{3} \left(\mathbf{J}_e \mathbf{J}_o^{-1}\right)_{x_k} \alpha_{kj} \\ &= \sum_{k=1}^{3} \left(\left(\mathbf{J}_e\right)_{x_k} \mathbf{J}_o^{-1} + \mathbf{J}_e \left(\mathbf{J}_o^{-1}\right)_{x_k} \right) \alpha_{kj}, \qquad j = 1,2,3 \end{aligned} \tag{9}$$

where $\left(\mathbf{J}_e\right)_{x_j} = \begin{bmatrix} \mathbf{r}_{x_1x_j} & \mathbf{r}_{x_2x_j} & \mathbf{r}_{x_3x_j} \end{bmatrix},\, j = 1,2,3$. Equation 9 defines the general expression for the curvature vectors. In the case of a surface, there are only three independent curvature vectors, while in the case of a volume, there are six independent curvature vectors. This is clear from the preceding equation since $\mathbf{r}_{X_kX_l} = \mathbf{r}_{X_lX_k},\, k,l = 1,2,3$.

4. Curvature constraints and Jacobian matrix

The general curvature expressions developed in the preceding section are defined with respect to the structure coordinates $\mathbf{X}$, and therefore, they can be used to impose the curvature constraint conditions at arbitrary points including the element nodes. These conditions automatically account for the gradient tensor transformation which can be used to define tangents to the same structure coordinate lines. Vector transformations normally used with conventional FE formulations are not appropriate when gradient and curvature vectors, which have a clear geometric meaning, are considered. Furthermore, the curvature expressions developed in this investigation allow for imposing curvature constraints without the need for imposing position and gradient continuity constraints, as it is the case when using the graphics-based B-splines and NURBS. This important ANCF feature provides the flexibility for developing general mechanics-based geometry/analysis algorithms that are necessary to address the CAE and durability-investigation challenges.

Using the general curvature expressions of Eq. 9, different curvature vectors can be equated at two arbitrary points on the same element or on two different elements of the ANCF mesh. For example, in the case of imposing curvature constraints at two points on two different elements i and j, one can write the curvature vector constraint equation as

$$\mathbf{r}^{i}_{X_k X_l} = \mathbf{r}^{j}_{X_m X_n}, \qquad k,l,m,n = 1,2,3 \tag{10}$$

While this vector equation defines three scalar equations, the algorithm can be designed in order to allow imposing curvature-continuity conditions on only scalar equations. In order to use the preceding constraint equations at a preprocessing stage to obtain the desired continuity conditions, eliminate the dependent variables, and obtain a reduced-order model, the *constraint Jacobian matrix* must be evaluated. To this end and after dropping the superscript that refers to the element number for simplicity, the curvature vectors $\mathbf{r}_{X_i X_j} = \partial^2 \mathbf{r} / \partial X_i \partial X_j$, $i,j = 1,2,3$, can be written as

$$\begin{aligned}
\mathbf{r}_{X_i X_j} &= \sum_{k=1}^{3} \left(\left(\mathbf{J}_e \right)_{x_k} \mathbf{C}_{Ji} + \mathbf{J}_e \mathbf{C}_{Jxi} \right) \alpha_{kj} \\
&= \sum_{k=1}^{3} \left(\alpha_{1i} \mathbf{r}_{x_1 x_k} + \alpha_{2i} \mathbf{r}_{x_2 x_k} + \alpha_{3i} \mathbf{r}_{x_3 x_k} + \alpha_{x_k 1i} \mathbf{r}_{x_1} + \alpha_{x_k 2i} \mathbf{r}_{x_2} + \alpha_{x_k 3i} \mathbf{r}_{x_3} \right) \alpha_{kj} \\
&= \sum_{k=1}^{3} \left(\alpha_{1i} \mathbf{r}_{x_1 x_k} + \alpha_{2i} \mathbf{r}_{x_2 x_k} + \alpha_{3i} \mathbf{r}_{x_3 x_k} \right) \alpha_{kj} + \sum_{k=1}^{3} \left(\alpha_{x_k 1i} \mathbf{r}_{x_1} + \alpha_{x_k 2i} \mathbf{r}_{x_2} + \alpha_{x_k 3i} \mathbf{r}_{x_3} \right) \alpha_{kj}
\end{aligned} \tag{11}$$

where $\alpha_{x_k lm}, l,m = 1,2,3$ is the lm th element of the matrix $\left(\mathbf{J}_o^{-1} \right)_{x_k}$, that is,

$$\left(\mathbf{J}_o^{-1} \right)_{x_k} = \begin{bmatrix} \alpha_{x_k 11} & \alpha_{x_k 12} & \alpha_{x_k 13} \\ \alpha_{x_k 21} & \alpha_{x_k 22} & \alpha_{x_k 23} \\ \alpha_{x_k 31} & \alpha_{x_k 32} & \alpha_{x_k 33} \end{bmatrix} \tag{12}$$

Because the displacement field of ANCF finite elements is defined as $\mathbf{r}(\mathbf{x},t)=\mathbf{S}(\mathbf{x})\mathbf{e}(t)$, the derivative of the curvature vectors with respect to the nodal coordinates $\mathbf{e}$ can then be evaluated as

$$\frac{\partial \mathbf{r}_{X_i X_j}}{\partial \mathbf{e}}=\sum_{k=1}^{3}\left(\alpha_{1i}\mathbf{S}_{x_1 x_k}+\alpha_{2i}\mathbf{S}_{x_2 x_k}+\alpha_{3i}\mathbf{S}_{x_3 x_k}\right)\alpha_{kj}+\sum_{k=1}^{3}\left(\alpha_{x_k 1i}\mathbf{S}_{x_1}+\alpha_{x_k 2i}\mathbf{S}_{x_2}+\alpha_{x_k 3i}\mathbf{S}_{x_3}\right)\alpha_{kj} \tag{13}$$

The shape function matrix $\mathbf{S}$ of an ANCF finite element can always be written as

$$\mathbf{S}(\mathbf{x})=\left[s_1(\mathbf{x})\mathbf{I} \quad s_2(\mathbf{x})\mathbf{I} \quad \cdots \quad s_{n_s}(\mathbf{x})\mathbf{I}\right] \tag{14}$$

where $s_k, k=1,2,\ldots,n_s$, are the shape functions, and n_s is the number of the element shape functions. The shape functions of the ANCF solid and tetrahedral elements used in this study are provided in the appendix of this paper. The first summation on the right hand-side of the preceding equation that defines $\partial \mathbf{r}_{X_i X_j} / \partial \mathbf{e}$ can be written as

$$\begin{aligned}\sum_{k=1}^{3}\left(\alpha_{1i}\mathbf{S}_{x_1 x_k}+\alpha_{2i}\mathbf{S}_{x_2 x_k}+\alpha_{3i}\mathbf{S}_{x_3 x_k}\right)\alpha_{kj} &=\sum_{k=1}^{3}\sum_{l=1}^{3}\alpha_{li}\alpha_{kj}\mathbf{S}_{x_l x_k}\\ &=\sum_{k=1}^{3}\sum_{l=1}^{3}\alpha_{li}\alpha_{kj}\left[\left(\left(s_1\right)_{x_l x_k}\right)\mathbf{I} \quad \left(\left(s_2\right)_{x_l x_k}\right)\mathbf{I} \quad \cdots \quad \left(\left(s_{ns}\right)_{x_l x_k}\right)\mathbf{I}\right]\end{aligned} \tag{15}$$

This equation can also be written as

$$\begin{aligned}\sum_{k=1}^{3}\left(\alpha_{1i}\mathbf{S}_{x_1 x_k}+\alpha_{2i}\mathbf{S}_{x_2 x_k}+\alpha_{3i}\mathbf{S}_{x_3 x_k}\right)\alpha_{kj} &=\sum_{k=1}^{3}\sum_{l=1}^{3}\alpha_{li}\alpha_{kj}\mathbf{S}_{x_l x_k}\\ &=\sum_{k=1}^{3}\sum_{l=1}^{3}\left[\left(\alpha_{li}\alpha_{kj}\left(s_1\right)_{x_l x_k}\right)\mathbf{I} \quad \left(\alpha_{li}\alpha_{kj}\left(s_2\right)_{x_l x_k}\right)\mathbf{I} \quad \cdots \quad \left(\alpha_{li}\alpha_{kj}\left(s_{ns}\right)_{x_l x_k}\right)\mathbf{I}\right]\end{aligned} \tag{16}$$

The second summation on the right hand-side of Eq. 13, which does not require the evaluation of the second derivatives of the shape function matrix with respect to the structural coordinates $\mathbf{X}$ can be also evaluated in a straight forward manner. Equation 13 defines the element of the constraint Jacobian matrix associated with the generalized coordinates of the finite element. The computations of the constraint Jacobian matrix is necessary in order to properly impose the curvature constraint conditions.

The form of Eq. 16 demonstrates clearly the effect of the geometry in the reference configuration on the shape functions when the curvature vectors are evaluated. Similar manipulations can also be made for the second summation on the right hand-side of Eq. 13 that defines the curvature Jacobian matrix $\partial \mathbf{r}_{X_i X_j} / \partial \mathbf{e}$. The equations developed in this section show the role of the matrix $\mathbf{J}_o$ which must be evaluated to properly account for the curved geometry in the reference configuration according to the continuum mechanics theory. It is, therefore, not clear how such a matrix can be systematically evaluated and used in developing general curvature equations when the graphics-based B-splines and NURBS are used in the analysis without destroying their structure. This raises questions on the appropriateness of using these graphics methods as analysis tools despite concerns on fundamental issues previously discussed in this study and in the literature [34].

It is important to point out that Ma.et al [27] examined the discontinuity problem of solid elements in the case of a flexible pendulum. They imposed continuity conditions using element coordinates to achieve C^1 continuity along x_1 at the solid element interface. In this paper, however, the general continuity conditions are formulated using structure coordinates to allow handling discontinuities when fully-parameterized ANCF elements have different orientations and have curved geometry in the reference-configuration.

5. Numerical investigation

As demonstrated in Section 2 of this paper, the standard FE assembly of ANCF fully-parameterized finite element ensures the continuity of the gradient vectors at the nodal points but does not ensure such a continuity for all gradients at the element interface. The discontinuity of the gradients at the element interface can adversely affect the strains and stress calculations, particularly in the case of soft and fluid materials. In the case of fluid materials, for example, the viscous stresses and forces are evaluated using the Naiver-Stokes equations which are expressed in terms of the time-rate of the position gradients. Gradient discontinuities at the element interface lead to discontinuities in the definitions of the viscous forces as well as in the accelerations. This is true since the viscous and elastic forces are normally evaluated at integration points and not only at nodal points. In this section, the effect of imposing the curvature-continuity conditions at the nodal points on the gradient continuity at the element interface is examined for both soft and fluid materials.

5.1 Solution procedure

The augmented form of the equations of motion of MBS systems that consist of rigid and flexible ANCF bodies can be written in terms of the system generalized reference and ANCF nodal coordinates $\mathbf{q}_r$ and $\mathbf{e}$, respectively. The nonlinear algebraic constraint equations are combined with the system differential equations of motion using the technique of Lagrange multipliers $\boldsymbol{\lambda}$. In general, the augmented form of the equations of motion can be written as

$$\begin{bmatrix} \mathbf{M}_r & \mathbf{0} & \mathbf{C}_{\mathbf{q}_r}^T \\ \mathbf{0} & \mathbf{M}_e & \mathbf{C}_{\mathbf{e}}^T \\ \mathbf{C}_{\mathbf{q}_r} & \mathbf{C}_{\mathbf{e}} & \mathbf{0} \end{bmatrix} \begin{bmatrix} \ddot{\mathbf{q}}_r \\ \ddot{\mathbf{e}} \\ \boldsymbol{\lambda} \end{bmatrix} = \begin{bmatrix} \mathbf{Q}_r \\ \mathbf{Q}_e \\ \mathbf{Q}_d \end{bmatrix} \tag{17}$$

where $\ddot{\mathbf{q}}_r$ and $\ddot{\mathbf{e}}$ are, respectively, the second time derivatives of the rigid body and ANCF element coordinates; $\mathbf{M}_r$ and $\mathbf{M}_e$ are, respectively, the mass matrices associated with the rigid body and ANCF element coordinates; $\mathbf{C}_{\mathbf{q}_r}$ and $\mathbf{C}_{\mathbf{e}}$ are, respectively, the constraint Jacobian matrices resulting from the differentiation with respect to the rigid body and ANCF coordinates; $\mathbf{Q}_r$ and

$\mathbf{Q}_e$ are, respectively, the vectors of generalized forces associated with the rigid body and ANCF nodal coordinates; and $\mathbf{Q}_d$ is a quadratic velocity vector that results from the differentiation of the constraint equations twice with respect to time. The solution of the preceding equation defines the generalized accelerations as well as the vector of Lagrange multipliers $\boldsymbol{\lambda}$, which can be used to determine the constraint forces [11].

Because the general continuity conditions are developed in this paper using linear algebraic equations, dependent variables resulting from imposing these conditions are eliminated at a preprocessing stage. Consequently, there is no need for using curvature formulations in the main processor, and as a result, the model dimension can be significantly reduced.

5.2 Soft material

The example used in this section is the same as the illustrative example used in Section 2.1 to introduce the gradient discontinuity problem at the interface. The results are obtained in this section by applying curvature-continuity conditions at the nodal points in order to examine the effect of such curvature-continuity conditions on the gradient continuity at the element interface. For the solid-element mesh, since only $\left(C^1\right)_{x_1}$ continuity is not ensured at the element interface, one can impose continuity of $\mathbf{r}_{X_1X_2}$ and $\mathbf{r}_{X_1X_3}$ curvature vectors at the interface nodal points. While for the tetrahedral-element mesh, $\left(C^1\right)_{x_1}$, $\left(C^1\right)_{x_2}$ and $\left(C^1\right)_{x_3}$ continuities are not ensured at the element interface, and therefore, the continuities of $\mathbf{r}_{X_iX_j}, i=j=1,2,3$ curvature vectors are imposed. The model material properties used in this numerical study are the density ρ=1500 $\mathrm{kg/m^3}$, and Young's modulus E=1.2 Mpa .

For the soft-material example considered in this section, it was found that the difference in the results of the gradient vector $\mathbf{r}_{x_1}$ at the interface point B obtained using the displacement fields of the two neighboring solid elements when the curvature-continuity conditions are imposed is of order 10^{-13}. This difference, when compared to the results presented in Fig. 3, can be used as measure of the degree of discontinuity and clearly demonstrates the significant effect of imposing the curvature-continuity conditions. The curvature-continuity conditions used for the solid-element model at a node k between two elements $i = E1$ and $j = E2$ are $\mathbf{r}^{ik}_{X_1X_2} = \mathbf{r}^{jk}_{X_1X_2}$, and $\mathbf{r}^{ik}_{X_1X_3} = \mathbf{r}^{jk}_{X_1X_3}$, $k = 2,3,6,7$. The curvature vectors are defined by differentiation with respect to the structure coordinates as previously explained in this paper. Therefore, twenty four linear algebraic curvature-continuity equations are imposed for the solid-element model, and consequently, the number of degrees of freedom of the model is reduced to 120. As previously discussed in this paper, the dependent variables as the result of imposing the curvature-continuity conditions can be eliminated at a preprocessing stage.

The differences, $\Delta\mathbf{r}_{x_j}\left(j\right), j = 1,2,3$, between the results obtained using the displacement fields of the two elements when using the tetrahedral-element model with the curvature-continuity conditions is of order 10^{-11}. For the five-tetrahedral-element mesh, the curvature constraints are imposed at the nodes of the interface surface between elements $i = E1$ (blue) and $j = E2$ (red) as shown in Fig. 2(b). The curvature constraints used for the tetrahedral-element model are $\mathbf{r}^{i3}_{X_1X_2} = \mathbf{r}^{j3}_{X_1X_2}, \mathbf{r}^{i3}_{X_1X_3} = \mathbf{r}^{j3}_{X_1X_3}, \mathbf{r}^{i3}_{X_2X_3} = \mathbf{r}^{j3}_{X_2X_3}$ for interface node 3 and $\mathbf{r}^{i5}_{X_1X_1} = \mathbf{r}^{j5}_{X_1X_1}, \mathbf{r}^{i5}_{X_2X_2} = \mathbf{r}^{j5}_{X_2X_2}$, $\mathbf{r}^{i5}_{X_3X_3} = \mathbf{r}^{j5}_{X_3X_3}$ for interface node 5; these conditions require the formulation of eighteen linear algebraic equations, and consequently the number of degrees of the tetrahedral-element model is reduced to seventy two.

Figures 5 – 8 show the displacement and velocity of the tip point A in the X_3 direction and Figs. 9 and 10 show the change in the normal strain at point B predicted using the solid- and tetrahedral-element models in the case of the soft material used in this section. The results presented in these figures demonstrate that imposing the curvature-continuity conditions can have an effect on the results, particularly in the case of the tetrahedral-element model. This can be attributed to the reduction in the number of degrees of freedom of the model, which in turn, can have an effect on the amount of energy absorbed due to the deformation of the soft materials.

5.3 Fluid material

In order to examine the effect of the curvature-continuity conditions on the behavior of the fluid material, the simple liquid-sloshing example shown in Fig. 11 is considered. The fluid, which is modeled using two simple ANCF solid- and tetrahedral-element meshes, is assumed to fill a cubic container subjected to a harmonic motion $x_1^c = 0.3\sin(3t)$ in the X_1 direction. The dimensions of cubic container are $a = b = c = 1\,\mathrm{m}$. The fluid is assumed to have mass density $\rho = 1000\,\mathrm{kg/m^3}$, and viscosity $\mu = 0.001\,\mathrm{Pa\cdot s}$; and the gravity effect is considered in this example. Figure 12 shows the first coordinate of the position-gradient vector $\mathbf{r}_{x_1}$ at point B predicted using the displacement fields of the two neighboring elements of the solid-element model when the curvature-continuity conditions are not imposed. It is clear from the results presented in this figure that this position-gradient vector is not continuous, and the difference in the first coordinate of this gradient vector $\Delta\mathbf{r}_{x_1}$ is shown in Fig. 13. Figure 14 shows the results obtained when applying the curvature constraints described in Section 5.1. It is clear from the results presented in this figure that the two elements predict the same gradient solution at the interface.

Figures 15 and 16 show the results obtained using the tetrahedral-element model without and with applying the curvature-continuity conditions, respectively. Comparing the results of these two figures show clearly the effect of the curvature-continuity constraints on the position gradients at the interface point B. It is noticed from the results presented in Figs. 15 and 16 that the differences in the magnitudes of gradients as predicted by the displacement fields of the two elements reduce when the curvature-continuity conditions are applied, and this contributes to achieving a higher degree of smoothness. Figures 17 shows fluid sloshing simulation at different time intervals using two-solid-element mesh without and with imposing the curvature constraints. This figure shows, as previously discussed in the introduction, that imposing the curvature constraints leads to improving the accuracy of the model and quality of the simulation results as well as to smoother free surface.

Figures 18 – 21 show the displacement and velocity of the mass center in the X_3 direction predicted using the solid and tetrahedral-element models. As in the case of the soft materials, the results presented in these figures show that imposing curvature-continuity conditions has more significant effect on the motion of the tetrahedral-element mesh as compared to the solid-element mesh. This can be attributed to the fact that the fluid constitutive model is function of the time-rate of the position-vector gradients, thereby, reducing the number of degrees of freedom of the model can have an impact on the energy absorbed by the deformation of the fluid material.

Figures 22 and 23 demonstrate the reduction in the difference between the gradient coordinates at point B by increasing the magnitude of the penalty coefficient for both solid and tetrahedral element models. These results show that, for incompressible materials, the effect of the discontinuities can be reduced because of the penalty force. The increase of the penalty coefficient, however, can lead to significant increase in the CPU time.

Figures 24 and 25 show the effect of number of elements on the gradient continuity when the curvature constraints are not imposed. For the solid element mesh, point C with the absolute position $\begin{bmatrix}0.5 & 0.25 & 0.5\end{bmatrix}^T$ is considered; while for the tetrahedral element mesh, point D with the absolute position $\begin{bmatrix}0.75 & 0.25 & 0\end{bmatrix}^T$ is considered. The results demonstrate that while mesh refinement can improve the gradient continuity, the discontinuity problem is not totally solved. Furthermore, increasing the mesh size leads to a larger model dimension that adversely affects the computational efficiency. On the other hand, the curvature constraints can solve the discontinuity problem without increasing the mesh size. This can be further demonstrated by performing a comparison between ANCF and conventional Lagrangian solid elements using the sloshing problem. The conventional element model is developed using the commercial software Ls-Dyna, in which the Lagrangian eight-node solid element is selected to develop the fluid model. The water constitutive model is defined using a "Null material" with Grüneisen equation of state [35]. The algorithm used to define the contact between the water and the container boundary is "Boundary_SPC", while the algorithm used for the container motion is "Boundary_Prescribed_Motion (BPM)" [36]. Figure 26 compares the tip X_3-displacement at the nodal point $\begin{bmatrix}1 & 1 & 1\end{bmatrix}^T$ obtained using ANCF and Ls-Dyna solutions. It is clear from the results presented in this figure that the two different models agree up to a certain point and start deviating as the displacement of the fluid increases due to the significant differences in the assumed displacement fields of the two elements and the achieved degrees of continuity. No curvature continuity constraints are applied to the ANCF model. The ANCF fluid models have been extensively tested, verified numerically, and validated experimentally [37, 38]. Therefore, the accuracy of the ANCF fluid solution for models that experience significant geometry changes and require a higher degree of smoothness to capture accurately such geometric changes has been evaluated. The results show that when using the two Lagrangian methods, the ANCF solution requires fewer elements to achieve a converged solution ($6 \times 6 \times 6$ elements) compared to the conventional FE method ($60 \times 60 \times 60$ elements) for this sloshing problem; demonstrating better convergence characteristics of ANCF finite elements in solving the fluid problem. Furthermore, if the curvature continuity conditions would be applied, the number of degrees of the freedom of the ANCF model would be further reduced while achieving a higher degree of smoothness at the element interface. Recent investigations by other authors have confirmed the advantages of using ANCF finite elements as compared to conventional finite elements in the analysis of sloshing problems [39].

6. Conclusions

In soft- and fluid-material applications including flexible and soft robots and liquid sloshing problems, continuity of the position gradients ensures continuity of the strains, stresses, and forces. Nonetheless, continuity of the position-vector gradients at the nodal points of an FE mesh does not ensure the continuity of these gradients at the element interfaces. Discontinuity of the gradients at the interface not only adversely affects strain, stress, and force calculations as well as the quality of the simulation results, but can also lead to computer models that do not properly represent realistic physical behaviors of the systems to be investigated. In this study, the ANCF finite elements are used to develop general *curvature-continuity* conditions that allow for eliminating or minimizing the discontinuity of the position gradients at the interfaces of the elements of an FE mesh. The general curvature-continuity conditions, which systematically account for both straight and curved geometries in the stress-free reference configuration, are developed without the need for using the CAD knot vector and knot multiplicity which do not properly account for the system degrees of freedom. The ANCF curvature-continuity conditions are expressed in terms of constant geometric coefficients defined using the matrix of position-vector gradients that describes the reference-configuration geometry. The formulation of these curvature-continuity conditions is demonstrated using the ANCF fully-parametrized three-dimensional solid and tetrahedral elements, which employ position gradients as nodal coordinates. The numerical results obtained in this investigation show that by applying the curvature-continuity conditions in the case of soft and fluid materials, higher degree of smoothness at the element interface can be achieved. Being able to adjust the degree of continuity of an FE mesh using a *mechanics-based approach* is necessary for the integration of geometry and analysis and for addressing the CAE- and durability-investigation challenges [31].

Appendix

In this appendix, the shape functions of the conventional tetrahedral, ANCF solid, and ANCF tetrahedral elements used in this study are presented.

A.1 Conventional tetrahedral element

For the conventional four-node (FN) tetrahedral element, the nodal coordinates $\mathbf{e}^k$ at node k are defined as

$$\mathbf{e}^k = \left(\mathbf{r}^k\right)^T, \qquad k=1,2,3,4 \tag{A.1}$$

where $\mathbf{r}^k$ is the global position vector of node k. The displacement field of each position coordinate of the element can be defined using a linear polynomial with four coefficients as $\phi(x_1, x_2, x_3) = \alpha_1 + \alpha_2 x_1 + \alpha_3 x_2 + \alpha_4 x_3$, where $\alpha_k, k = 1,2,3,4$, are the polynomial coefficients. The position vector of an arbitrary material point on element can be written as $\mathbf{r} = \mathbf{N}\mathbf{e}$, where $\mathbf{N}$ is the shape function matrix and $\mathbf{e}$ is the vector of the nodal coordinates, which can be written respectively as

$$\left.\begin{aligned} \mathbf{N} &= \begin{bmatrix} N_1\mathbf{I} & N_2\mathbf{I} & N_3\mathbf{I} & N_4\mathbf{I} \end{bmatrix} \\ \mathbf{e} &= \begin{bmatrix} \left(\mathbf{e}^1\right)^T & \left(\mathbf{e}^2\right)^T & \left(\mathbf{e}^3\right)^T & \left(\mathbf{e}^4\right)^T \end{bmatrix}^T \end{aligned}\right\} \tag{A.2}$$

where $\mathbf{I}$ is the 3×3 identity matrix. The conventional FN tetrahedral element has twelve degrees of freedom, and the shape functions $N_k, k = 1,2,3,4$, are defined in a closed form as,

$$N_k = \frac{1}{6V}\left(a_k + b_k x_1 + c_k x_2 + d_k x_3\right), \quad k = 1,2,3,4 \tag{A.3}$$

where V is the volume of the element, and a_k, b_k, c_k, d_k are defined as

$$
\begin{aligned}
a_k &= (-1)^{k+1}\begin{vmatrix} x_{1m} & x_{2m} & x_{3m} \\ x_{1n} & x_{2n} & x_{3n} \\ x_{1p} & x_{2p} & x_{3p} \end{vmatrix}, \qquad b_k = (-1)^{k}\begin{vmatrix} 1 & x_{2m} & x_{3m} \\ 1 & x_{2n} & x_{3n} \\ 1 & x_{2p} & x_{3p} \end{vmatrix} \\
c_k &= (-1)^{k+1}\begin{vmatrix} x_{1m} & 1 & x_{3m} \\ x_{1n} & 1 & x_{3n} \\ x_{1p} & 1 & x_{3p} \end{vmatrix}, \qquad d_k = (-1)^{k}\begin{vmatrix} x_{1m} & x_{2m} & 1 \\ x_{1n} & x_{2n} & 1 \\ x_{1p} & x_{2p} & 1 \end{vmatrix}
\end{aligned}
\tag{A.4}
$$

where m, n, p are the other three node numbers that are different from node k, arranged according to the sequence used for this element.

A.2 ANCF solid element

For the ANCF solid element, the coordinates $\mathbf{e}^k$ at node k are defined as [6, 29]

$$
\mathbf{e}^k = \left[\left(\mathbf{r}^k\right)^T \quad \left(\mathbf{r}^k_{x_1}\right)^T \quad \left(\mathbf{r}^k_{x_2}\right)^T \quad \left(\mathbf{r}^k_{x_3}\right)^T \right]^T, \quad k = 1, 2, ..., 8 \tag{A.5}
$$

where $\mathbf{r}^k$ is the global position vector of node k, and $\mathbf{r}^k_{x_1}$, $\mathbf{r}^k_{x_2}$, and $\mathbf{r}^k_{x_3}$ are the position-gradient vectors obtained by differentiation with respect to the spatial coordinates x_1, x_2, and x_3, respectively. The interpolating polynomial of each position coordinate of the ANCF solid element is defined using thirty two coefficients as

$$
\begin{aligned}
\phi(x_1, x_2, x_3) = {} & \alpha_1 + \alpha_2 x_1 + \alpha_3 x_2 + \alpha_4 x_3 + \alpha_5 x_1^2 + \alpha_6 x_2^2 + \alpha_7 x_3^2 \\
& + \alpha_8 x_1 x_2 + \alpha_9 x_2 x_3 + \alpha_{10} x_1 x_3 + \alpha_{11} x_1^3 + \alpha_{12} x_2^3 + \alpha_{13} x_3^3 \\
& + \alpha_{14} x_1^2 x_2 + \alpha_{15} x_1^2 x_3 + \alpha_{16} x_2^2 x_3 + \alpha_{17} x_1 x_2^2 + \alpha_{18} x_1 x_3^2 \\
& + \alpha_{19} x_2 x_3^2 + \alpha_{20} x_1 x_2 x_3 + \alpha_{21} x_1^3 x_2 + \alpha_{22} x_1^3 x_3 + \alpha_{23} x_1 x_2^3 \\
& + \alpha_{24} x_2^3 x_3 + \alpha_{25} x_1 x_3^3 + \alpha_{26} x_2 x_3^3 + \alpha_{27} x_1^2 x_2 x_3 + \alpha_{28} x_1 x_2^2 x_3 \\
& + \alpha_{29} x_1 x_2 x_3^2 + \alpha_{30} x_1^3 x_2 x_3 + \alpha_{31} x_1 x_2^3 x_3 + \alpha_{32} x_1 x_2 x_3^3
\end{aligned}
\tag{A.6}
$$

where $\alpha_i, i = 1, 2, \ldots, 32$ are the polynomial coefficients. The position vector of an arbitrary material point on element can be written as $\mathbf{r} = \sum_{k=1}^{8} \left[S^{k,1}\mathbf{I} \quad S^{k,2}\mathbf{I} \quad S^{k,3}\mathbf{I} \quad S^{k,4}\mathbf{I} \right] \mathbf{e}^k = \mathbf{Se}$, where $\mathbf{S}$ is the shape function matrix and $\mathbf{e}$ is the vector of the nodal coordinates defined, respectively, as

$$\left.\begin{aligned}\mathbf{S} &= \begin{bmatrix} s^{1,1}\mathbf{I} & s^{1,2}\mathbf{I} & s^{1,3}\mathbf{I} & s^{1,4}\mathbf{I} & \ldots & s^{8,1}\mathbf{I} & s^{8,2}\mathbf{I} & s^{8,3}\mathbf{I} & s^{8,4}\mathbf{I} \end{bmatrix} \\ \mathbf{e} &= \begin{bmatrix} (\mathbf{e}^1)^T & (\mathbf{e}^2)^T & (\mathbf{e}^3)^T & (\mathbf{e}^4)^T & (\mathbf{e}^5)^T & (\mathbf{e}^6)^T & (\mathbf{e}^7)^T & (\mathbf{e}^8)^T \end{bmatrix}^T \end{aligned}\right\} \tag{A.7}$$

where $\mathbf{I}$ is the 3×3 identity matrix. The ANCF solid element has ninety six degrees of freedom, and the shape functions of the element are defined in a closed form as

$$\left.\begin{aligned} & s^{k,1} = (-1)^{1+\xi_k+\eta_k+\zeta_k}(\xi+\xi_k-1)(\eta+\eta_k-1)(\zeta+\zeta_k-1)\cdot \\ & \left(1+(\xi-\xi_k)(1-2\xi)+(\eta-\eta_k)(1-2\eta)+(\zeta-\zeta_k)(1-2\zeta)\right) \\ & s^{k,2} = (-1)^{\eta_k+\zeta_k} a\xi^{\xi_k+1}(\xi-1)^{2-\xi_k}\eta^{\eta_k}(\eta-1)^{1-\eta_k}\zeta^{\zeta_k}(\zeta-1)^{1-\zeta_k} \\ & s^{k,3} = (-1)^{\xi_k+\zeta_k} b\xi^{\xi_k+1}(\xi-1)^{1-\xi_k}\eta^{\eta_k+1}(\eta-1)^{2-\eta_k}\zeta^{\zeta_k}(\zeta-1)^{1-\zeta_k} \\ & s^{k,4} = (-1)^{\xi_k+\eta_k} c\xi^{\xi_k+1}(\xi-1)^{1-\xi_k}\eta^{\eta_k}(\eta-1)^{1-\eta_k}\zeta^{\zeta_k+1}(\zeta-1)^{2-\zeta_k} \end{aligned}\right\} \tag{A.8}$$
$$k = 1,2,\ldots,8$$

where a,b, and c are the dimensions of the element in the x_1, x_2, and x_3 directions, $\xi = x_1/a, \eta = x_2/b, \zeta = x_3/c$, $\xi,\eta,\zeta \in [0,1]$, and ξ_k,η_k,ζ_k are the dimensionless nodal coordinates for node k.

For a given a given value for the coordinate x, one can show that the interpolation of Eq. A.6 reduces to

$$\begin{aligned}\phi(x_1,x_2,x_3) = {} & \alpha_1 + \alpha_2 x_2 + \alpha_3 x_3 + \alpha_4 x_2^2 + \alpha_5 x_3^2 + \alpha_6 x_2 x_3 + \alpha_7 x_2^3 \\ & + \alpha_8 x_3^3 + \alpha_9 x_2^2 x_3 + \alpha_{10} x_2 x_3^2 + \alpha_{11} x_2^3 x_3 + \alpha_{12} x_2 x_3^3 \end{aligned} \tag{A.9}$$

This two-parameter cubic interpolation has twelve coefficients, and therefore, imposing continuity on $\mathbf{r}, \mathbf{r}_{x_2}$, and $\mathbf{r}_{x_3}$ at the nodal points will ensure the continuity of the gradients $\mathbf{r}_{x_2}$ and $\mathbf{r}_{x_3}$ at the element interface surfaces as discussed in this paper.

For a given a given value for the coordinate x_1, one can show that the interpolation of Eq. A.6 reduces to

$$\begin{aligned}\phi(x_1,x_2,x_3) = \alpha_1 + \alpha_2 x_2 + \alpha_3 x_3 + \alpha_4 x_2^2 + \alpha_5 x_3^2 + \alpha_6 x_2 x_3 + \alpha_7 x_2^3 \\ + \alpha_8 x_3^3 + \alpha_9 x_2^2 x_3 + \alpha_{10} x_2 x_3^2 + \alpha_{11} x_2^3 x_3 + \alpha_{12} x_2 x_3^3\end{aligned} \tag{A.9}$$

This two-parameter cubic interpolation has twelve coefficients, and therefore, imposing continuity on $\mathbf{r},\mathbf{r}_{x_2}$, and $\mathbf{r}_{x_3}$ at the nodal points will ensure the continuity of the gradients $\mathbf{r}_{x_2}$ and $\mathbf{r}_{x_3}$ at the element interface surfaces as discussed in this paper.

A.3 ANCF tetrahedral element

For the ANCF four-node (FN) tetrahedral element, the vector of the element nodal coordinates can be written as [30]

$$\begin{aligned}\mathbf{e} = \Big[& (\mathbf{r}^1)^T \quad (\mathbf{r}_\eta^1)^T \quad (\mathbf{r}_\zeta^1)^T \quad (\mathbf{r}_\chi^1)^T \quad (\mathbf{r}^2)^T \quad (\mathbf{r}_\zeta^2)^T \quad (\mathbf{r}_\chi^2)^T \quad (\mathbf{r}_\xi^2)^T \\ & (\mathbf{r}^3)^T \quad (\mathbf{r}_\chi^3)^T \quad (\mathbf{r}_\xi^3)^T \quad (\mathbf{r}_\eta^3)^T \quad (\mathbf{r}^4)^T \quad (\mathbf{r}_\xi^4)^T \quad (\mathbf{r}_\eta^4)^T \quad (\mathbf{r}_\zeta^4)^T \Big]^T\end{aligned} \tag{A.10}$$

where $\mathbf{r}^k$ is the global position vector of node k of the element, and $\mathbf{r}_\xi^k = \partial \mathbf{r}^k / \partial \xi$, $\mathbf{r}_\eta^k = \partial \mathbf{r}^k / \partial \eta$, $\mathbf{r}_\zeta^k = \partial \mathbf{r}^k / \partial \zeta$, $\mathbf{r}_\chi^k = \partial \mathbf{r}^k / \partial \chi$, $k = 1,2,3,4$, are the position-gradient vectors obtained by differentiation with respect to the volume coordinates ξ,η,ζ, and χ, respectively. The ANCF FN tetrahedral element assumed displacement field is defined using a cubic Bezier tetrahedral patch with twenty basis polynomials and four linear constraints [30]. The twenty Bezier basis functions are

$$\left.\begin{array}{c} g_1 = \xi^3, \quad g_2 = \eta^3, \quad g_3 = \zeta^3, g_4 = \chi^3 \\ g_5 = 3\xi^2\eta, \quad g_6 = 3\xi\eta^2, \quad g_7 = 3\eta^2\zeta, \quad g_8 = 3\eta\zeta^2 \\ g_9 = 3\xi^2\zeta, \quad g_{10} = 3\xi\zeta^2, \quad g_{11} = 3\xi^2\chi, \quad g_{12} = 3\xi\chi^2 \\ g_{13} = 3\eta^2\chi, \quad g_{14} = 3\eta\chi^2, \quad g_{15} = 3\zeta^2\chi, \quad g_{16} = 3\zeta\chi^2 \\ g_{17} = 6\xi\eta\zeta, \quad g_{18} = 6\xi\eta\chi, \quad g_{19} = 6\eta\zeta\chi, \quad g_{20} = 6\xi\zeta\chi \end{array}\right\} \tag{A.11}$$

Using the four linear constraint equations [30], the displacement field of the ANCF FN tetrahedral element can be defined using sixteen polynomials. The position vector of an arbitrary material point on element can be written as $\mathbf{r} = \mathbf{S}\mathbf{e}$, where $\mathbf{S}$ is the shape function matrix and $\mathbf{e}$ is the vector of the nodal coordinates defined, respectively, as

$$\left.\begin{aligned}\mathbf{S} &= \left[s_1\mathbf{I} \quad s_2\mathbf{I} \quad s_3\mathbf{I} \quad s_4\mathbf{I} \quad s_5\mathbf{I} \quad s_6\mathbf{I} \quad s_7\mathbf{I} \quad s_8\mathbf{I}\right. \\ &\qquad \left. s_9\mathbf{I} \quad s_{10}\mathbf{I} \quad s_{11}\mathbf{I} \quad s_{12}\mathbf{I} \quad s_{13}\mathbf{I} \quad s_{14}\mathbf{I} \quad s_{15}\mathbf{I} \quad s_{16}\mathbf{I}\right] \\ \mathbf{e} &= \left[\left(\mathbf{e}^1\right)^T \quad \left(\mathbf{e}^2\right)^T \quad \left(\mathbf{e}^3\right)^T \quad \left(\mathbf{e}^4\right)^T\right]^T\end{aligned}\right\} \tag{A.12}$$

where $\mathbf{I}$ is the 3×3 identity matrix. The ANCF FN tetrahedral element has forty eight degrees of freedom, and its shape functions are defined in a closed form as

$$\left.\begin{aligned}&s_1 = \xi\left(\xi^2 + 3\xi\left(\eta+\zeta+\chi\right) + 2\left(\eta\zeta + \chi\left(\eta+\zeta\right)\right)\right), \quad s_2 = \frac{1}{3}\xi\eta\left(3\xi-\zeta-\chi\right), \quad s_3 = \frac{1}{3}\xi\zeta\left(3\xi-\chi-\eta\right), \\ &s_4 = \frac{1}{3}\xi\chi\left(3\xi-\eta-\zeta\right), \quad s_5 = \eta\left(\eta^2 + 3\eta\left(\zeta+\chi+\xi\right) + 2\left(\zeta\chi + \xi\left(\zeta+\chi\right)\right)\right), \quad s_6 = \frac{1}{3}\eta\zeta\left(3\eta-\chi-\xi\right), \\ &s_7 = \frac{1}{3}\eta\chi\left(3\eta-\xi-\zeta\right), \quad s_8 = \frac{1}{3}\eta\xi\left(3\eta-\zeta-\chi\right), \quad s_9 = \zeta\left(\zeta^2 + 3\zeta\left(\chi+\xi+\eta\right) + 2\left(\chi\xi + \eta\left(\chi+\xi\right)\right)\right), \\ &s_{10} = \frac{1}{3}\zeta\chi\left(3\zeta-\xi-\eta\right), \quad s_{11} = \frac{1}{3}\zeta\xi\left(3\zeta-\eta-\chi\right), \quad s_{12} = \frac{1}{3}\zeta\eta\left(3\zeta-\chi-\xi\right), \\ &s_{13} = \chi\left(\chi^2 + 3\chi\left(\xi+\eta+\zeta\right) + 2\left(\xi\eta + \zeta\left(\xi+\eta\right)\right)\right), \quad s_{14} = \frac{1}{3}\chi\xi\left(3\chi-\eta-\zeta\right), \\ &s_{15} = \frac{1}{3}\chi\eta\left(3\chi-\zeta-\xi\right), \quad s_{16} = \frac{1}{3}\chi\zeta\left(3\chi-\xi-\eta\right)\end{aligned}\right\} \tag{A.13}$$

A surface, in general, can be described in terms of two parameters s_1 and s_2, using the following parametric form [25, 26],

$$\mathbf{r}\left(s_1, s_2\right) = \left[r_1\left(s_1,s_2\right) \quad r_2\left(s_1,s_2\right) \quad r_3\left(s_1,s_2\right)\right]^T \tag{A.14}$$

The surface Jacobian matrix defined by differentiation with respect to the parameters s_1 and s_2 is,

$$\mathbf{J}_s = \begin{bmatrix}\dfrac{\partial \mathbf{r}}{\partial s_1} & \dfrac{\partial \mathbf{r}}{\partial s_2}\end{bmatrix} = \begin{bmatrix}\mathbf{r}_{s_1} & \mathbf{r}_{s_2}\end{bmatrix} = \begin{bmatrix}\dfrac{\partial r_1}{\partial s_1} & \dfrac{\partial r_1}{\partial s_2} \\ \dfrac{\partial r_2}{\partial s_1} & \dfrac{\partial r_2}{\partial s_2} \\ \dfrac{\partial r_3}{\partial s_1} & \dfrac{\partial r_3}{\partial s_2}\end{bmatrix} \tag{A.15}$$

This matrix has rank equal to two, and the condition $\mathbf{r}_{s_1} \times \mathbf{r}_{s_2} \neq \mathbf{0}$ must be satisfied.

The relationship between the Cartesian gradients $\mathbf{r}_{X_j}$ and the surface gradients $\mathbf{r}_{s_i}$ is

$$\mathbf{J}_s = \mathbf{r}_{s_i} = \frac{\partial \mathbf{r}_j}{\partial \mathbf{s}_i} = \frac{\partial \mathbf{r}_j}{\partial \mathbf{X}_j}\frac{\partial \mathbf{X}_j}{\partial \mathbf{s}_i} = \mathbf{J}\frac{\partial \mathbf{X}_j}{\partial \mathbf{s}_i} = \mathbf{r}_{X_j}\mathbf{C}_{Jsi} \qquad i = 1,2 \quad j = 1,2,3 \tag{A.16}$$

where, $\mathbf{C}_{Jsi} = \partial \mathbf{X}_j / \partial \mathbf{s}_i$ is a 3×2 transformation matrix defined as

$$\mathbf{C}_{Jsi} = \begin{bmatrix} \dfrac{\partial X_1}{\partial s_1} & \dfrac{\partial X_1}{\partial s_2} \\ \dfrac{\partial X_2}{\partial s_1} & \dfrac{\partial X_2}{\partial s_2} \\ \dfrac{\partial X_3}{\partial s_1} & \dfrac{\partial X_3}{\partial s_2} \end{bmatrix} \tag{A.17}$$

At the nodes, the Cartesian gradients $\mathbf{r}_{X_j}$ are continuous, therefore, the surface gradients $\mathbf{r}_{s_i}$ tangent to the element interface surface are also continuous due to the gradient transformation. Use of cubic interpolation with ten polynomial coefficients requires imposing ten conditions to ensure that the interface surfaces of the two elements are the same. Because only nine continuity conditions result from $\mathbf{r}, \mathbf{r}_{s_1}$, and $\mathbf{r}_{s_2}$ of the three nodes, they are not sufficient to ensure that the two interface surfaces of the two elements have the same geometry.

Acknowledgments

This research was supported by the National Science Foundation (Projects # 1632302 and 1852510).

Compliance with Ethical Standards:

The authors declare that they have no conflict of interest

References

1. Yang, S., Deng, Z., Sun, J., Zhao, Y., and Jiang, S., 2018, "An Improved Variable-Length Beam Element with a Torsion Effect Based on the Absolute Nodal Coordinate Formulation", *IMechE Journal of Multibody Dynamics*, Vol. 232, pp. 69 – 83.
2. Dmitrochenko, O. N, and Pogorelov, D. Y., 2003, "Generalization of Plate Finite Elements for Absolute Nodal Coordinate Formulation", *Multibody System Dynamics*, 10, pp 17-43.
3. Gerstmayr, J., and Irschik, H., 2008, "On the Correct Representation of Bending and Axial Deformation in the Absolute Nodal Coordinate Formulation with an Elastic Line Approach," *Journal of Sound & Vibration*, 318(3), pp. 461-487.
4. Hu, W., Tian, Q., and Hu, H. Y., 2014, "Dynamics Simulation of the Liquid-Filled Flexible Multibody System via the Absolute Nodal Coordinate Formulation and SPH Method", *Nonlinear Dynamics*, Vol. 75, pp.653-671.
5. Nachbagauer, K., 2014, "State of the Art of ANCF Elements Regarding Geometric Description, Interpolation strategies, Definition of Elastic Forces, Validation and Locking Phenomenon in Comparison with Proposed Beam Finite Elements," *Archives of Computational Methods in Engineering*, 21(3), pp. 293-319.
6. Olshevskiy, A., Dmitrochenko, O., and Kim, C.W., 2014, "Three-Dimensional Solid Brick Element using Slopes in the Absolute Nodal Coordinate Formulation," *ASME Journal of Computational & Nonlinear Dynamics*, 9(2), pp. 1-10.
7. Orzechowski, G., and Fraczek, J., 2015, "Nearly Incompressible Nonlinear Material Models in the Large Deformation Analysis of Beams using ANCF," *Nonlinear Dynamics*, 82(1), pp. 451-464.

8. Tian, Q., Chen, L.P., Zhang, Y.Q., and Yang, J.Z., 2009, "An Efficient Hybrid Method for Multibody Dynamics Simulation Based on Absolute Nodal Coordinate Formulation", *ASME Journal of Computational and Nonlinear Dynamics*, Vol. 4, pp. 021009-1 - 021009-14.
9. Tian, Q., Sun, Y. L., Liu, C., Hu, H. Y., and Paulo, F., 2013, "Elasto-Hydro-Dynamic Lubricated Cylindrical Joints for Rigid-Flexible Multibody Dynamics", *Computers & Structures*, Vol. 114-115, pp. 106 - 120.
10. Shen, Z., Li, P., Liu, C., and Hu, G., 2014, "A Finite Element Beam Model Including Cross-Section Distortion in the Absolute Nodal Coordinate Formulation," *Nonlinear Dynamics*, 77(3), pp. 1019-1033.
11. Shabana, A.A., 2018, *Computational Continuum Mechanics*, Third Edition, Cambridge University Press, Cambridge.
12. Shabana, A.A., 2015, "Definition of ANCF Finite Elements", *ASME Journal of Computational and Nonlinear Dynamics*, Vol. 10, pp. 054506-1 - 054506-5.
13. Bonet, J., and Wood, R.D., 1997, *Nonlinear Continuum Mechanics for Finite Element Analysis*, Cambridge University Press.
14. Bathe, K. J., 1996, *Finite Element Procedures*, Prentice Hall, Englewood Cliffs, NJ.
15. Cook, R.D., Malkus, D.S., and Plesha, M.E., 1989, *Concepts and Applications of Finite Element Analysis*, Third Edition, John Wiley & Sons.
16. Crisfield, M.A., 1991, *Nonlinear Finite Element Analysis of Solids and Structures, Vol. 1: Essentials*, John Wiley & Sons.
17. Zienkiewicz, O.C., 1977, *The Finite Element Method*, Third Edition, McGraw Hill, New York.
18. Zienkiewicz, O.C., and Taylor, R.L., 2000, *The Finite Element Method, Vol. 2: Solid Mechanics*, Fifth Edition, Butterworth Heinemann.

19. White, F. M., 2003, *Fluid Mechanics*, 5th Edition, McGraw Hill, New York.

20. Farin, G., 1999, *Curves and Surfaces for CAGD*, A Practical Guide, Fifth Edition, Morgan Kaufmann, Publishers, San Francisco.

21. Piegl. L., Tiller. W., 1997, *The NURBS Book*, Second Edition, Springer, New York.

22. Rogers, D.F., 2001, *An Introduction to NURBS With Historical Perspective*, Academic Press, San Diego, CA.

23. Gallier, J., 2011, *Geometric Methods and Applications: For Computer Science and Engineering*, Springer, New York.

24. Gibson, S.F.F., and Mirtich, B., 1997, "A Survey of Deformable Modeling in Computer Graphics", Mitsubishi Electric Research Laboratories, (http://www.merl.com), TR97-19.

25. Goetz, A., 1970, *Introduction to Differential Geometry*, Addison Wesley.

26. Kreyszig, E., 1991, *Differential Geometry*, Dover Publications.

27. Ma, C., Wang, R., Wei, C., and Zhao, Y., 2016, "A New Absolute Nodal Coordinate Formulation of Solid Element with Continuity Condition and Viscosity Model", *International Journal of Simulation: Systems, Science and Technology*, Vol. 17(21), pp 10.1–10.6.

28. Metaxas, D.N., 2012, *Physics-Based Deformable Models: Applications to Computer Vision, Graphics, and Medical Imaging*, Springer, New York.

29. Metaxas, D., and Terzopoulos, D., 1993, "Shape and Nonrigid Motion Estimation through Physics-Based Synthesis", *IEEE transactions on Pattern Analysis and Machine Intelligence*, Vol. 15, pp. 580 – 591.

30. Qin, H., and Terzopoulos, D., 1996, "D-NURBS: A Physics-Based Framework for Geometric Design", *IEEE Transactions on Visualization and Computer Graphics*, Vol. 2(1), pp. 85–96.

31. Terzopoulos, D., and Metaxas, D., 1991, "Dynamic 3D Models with Local and Global Deformations: Deformable Superquadrics", *IEEE transactions on Pattern Analysis and Machine Intelligence*, Vol. 13, pp. 703 – 714.

32. Wei, C., Wang, L., and Shabana, A.A., 2015, "A Total Lagrangian ANCF Liquid Sloshing Approach for Multibody System Applications", *ASME Journal of Computational and Nonlinear Dynamics*, Vol. 10, pp. 051014-1 - 051014-10.

33. Pappalardo, C.M., Wang, T., and Shabana, A.A., 2017, "Development of ANCF Tetrahedral Finite Elements for the Nonlinear Dynamics of Flexible Structures", *Nonlinear Dynamics*, Vol. 89, pp 2905–2932.

34. Shabana, A.A., 2019, "Integration of Computer-Aided Design and Analysis (I-CAD-A): Application to Multibody Vehicle Systems", *International Journal of Vehicle Performance*, Vol. 5, pp. 300 - 327.

35. Grüneisen, E., 1912, "Theorie des Festen Zustandes Einatomiger Elemente," *Ann. Phys*. 344(12), pp.257–306.

36. LS-DYNA© Keyword User's Manual—LSTC (2018).

37. Grossi, E., Shabana, A.A., 2017, "Validation of a Total Lagrangian ANCF Solution Procedure for Fluid–Structure Interaction Problems", *ASME J. Verif. Valid. Uncertain. Quantif*, Vol. 2(4), pp. 041001-1-041001-13.

38. Mohammed M. A, Shi, S., Grossi, E., Shabana, A.A., 2019, "Evaluation of Breaking Wave Effects in Liquid Sloshing Problems: ANCF/SPH Comparative Study", *Nonlinear Dyn*, Vol. 97(1), pp. 45-62.

39. Ma, L., Wei, C., and Zhao, Y., 2020, “Modeling and Verification of a RANCF Fluid Element Based on Cubic Rational Bezier Volume”, *ASME Journal of Computational and Nonlinear Dynamics*, (in press).

LIST OF FIGURE CAPTIONS

Figure 1. ANCF element (a) ANCF solid element, (b) ANCF tetrahedral element

Figure 2. Flexible pendulum (a) ANCF solid-element mesh, (b) ANCF tetrahedral-element mesh

Figure 3. Gradient coordinate at point B predicted using ANCF solid element in the case of soft material without curvature constraints

Figure 4. Difference in the gradient coordinates at point B when using ANCF tetrahedral element in the case of soft material without curvature constraints
($\Delta \mathbf{r}_{x_1}$ (1), $\Delta \mathbf{r}_{x_2}$ (2), $\Delta \mathbf{r}_{x_3}$ (3))

Figure 5. X_3-displacement of tip point A using in the case of soft material predicted using ANCF solid-element mesh
(Without curvature constraints, With curvature constraints)

Figure 6. X_3-displacement of tip point A in the case of soft material using ANCF tetrahedral-element mesh
(Without curvature constraints, With curvature constraints)

Figure 7. Velocity of tip point A using in the X_3 direction in the case of soft material predicted using ANCF solid-element mesh
(Without curvature constraints, With curvature constraints)

Figure 8. Velocity of tip point A using in the X_3 direction in the case of soft material predicted using ANCF tetrahedral-element mesh
(Without curvature constraints, With curvature constraints)

Figure 9. Normal strain change at point B when using ANCF solid element in the case of soft material
((a). Without curvature constraints, (b). With curvature constraints)
($\varepsilon_{x_1x_1}$, $\varepsilon_{x_2x_2}$, $\varepsilon_{x_3x_3}$), (Element 1, Element 2)

Figure 10. Normal strain change at point B when using ANCF tetrahedral element in the case of soft material
((a). Without curvature constraints, (b). With curvature constraints)
($\varepsilon_{x_1x_1}$, $\varepsilon_{x_2x_2}$, $\varepsilon_{x_3x_3}$), (Element 1, Element 2)

Figure 11. Fluid sloshing example (a) ANCF solid-element mesh, (b) ANCF tetrahedral-element mesh

Figure 12. Gradient coordinate at point B predicted using ANCF solid element in the case of fluid material without curvature constraints

(Element 1, Element 2)

Figure 13. Difference in the gradient coordinate at point B predicted using ANCF solid element in the case of fluid material without curvature constraints

Figure 14. Gradient coordinate at point B predicted using ANCF solid element in the case of fluid material with curvature constraints
(Element 1, Element 2)

Figure 15. Gradient coordinates at point B predicted using ANCF tetrahedral element in the case of fluid material without curvature constraints
($\mathbf{r}_{x_1}(1)$, $\mathbf{r}_{x_2}(2)$, $\mathbf{r}_{x_3}(3)$), (Element 1, Element 2)

Figure 16. Gradient coordinates at point B predicted using ANCF tetrahedral element in the case of fluid material with curvature constraints
($\mathbf{r}_{x_1}(1)$, $\mathbf{r}_{x_2}(2)$, $\mathbf{r}_{x_3}(3)$), (Element 1, Element 2)

Figure 17. Fluid deformed shape using ANCF solid-element mesh
(a) Without curvature constraints, (b) With curvature constraints

Figure 18. Mass-center X_3-displacement in the case of fluid material predicted using ANCF solid-element mesh
(Without curvature constraints, With curvature constraints)

Figure 19. Mass-center X_3-displacement in the case of fluid material predicted using ANCF tetrahedral-element mesh
(Without curvature constraints, With curvature constraints)

Figure 20. Mass-center X_3-velocity in the case of fluid material predicted using ANCF solid-element mesh
(Without curvature constraints, With curvature constraints)

Figure 21. Mass-center X_3-velocity in the case of fluid material predicted using ANCF tetrahedral-element mesh
(Without curvature constraints, With curvature constraints)

Figure 22. Influence of penalty coefficient on the gradient coordinate difference at point B when using ANCF solid element in the case of fluid material without curvature constraints
($k_{IC} = 1\times10^7$, $k_{IC} = 1\times10^8$)

Figure 23. Influence of penalty coefficient on the gradient coordinate difference at point B when using ANCF tetrahedral element in the case of fluid material without curvature constraints
($\Delta\mathbf{r}_{x_1}(1)$, $\Delta\mathbf{r}_{x_2}(2)$, $\Delta\mathbf{r}_{x_3}(3)$), ($k_{IC} = 1\times10^7$, $k_{IC} = 1\times10^8$)

Figure 24. Influence of mesh size on the gradient coordinate difference at point C when using ANCF solid element in the case of fluid material
(2 elements, 8 elements)

Figure 25. Influence of mesh size on the gradient coordinate difference at point D when using ANCF tetrahedral element in the case of fluid material
($\Delta\mathbf{r}_{x_1}(1)$, $\Delta\mathbf{r}_{x_2}(2)$, $\Delta\mathbf{r}_{x_3}(3)$)
(2 elements, 5 elements, 40 Elements)

Figure 26. Comparison test in the case of ANCF solid element and LsDyna solid element
(ANCF $4\times4\times4$ elements, ANCF $5\times5\times5$ elements, ANCF $6\times6\times6$ elements; Ls-Dyna $40\times40\times40$ elements, Ls-Dyna $50\times50\times50$ elements, Ls-Dyna $60\times60\times60$ elements)

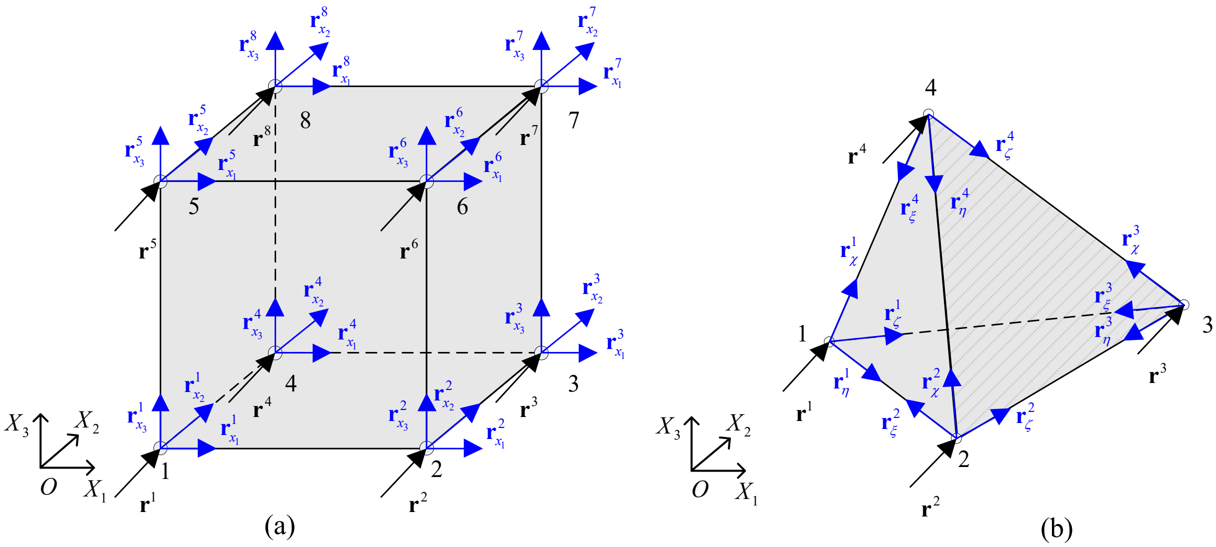

Figure 1. ANCF element
(a) ANCF solid element, (b) ANCF tetrahedral element

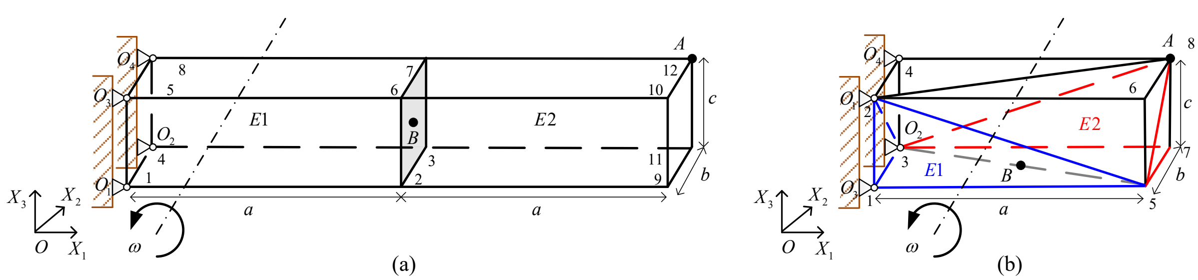

Figure 2. Flexible pendulum
(a) ANCF solid-element mesh, (b) ANCF tetrahedral-element mesh

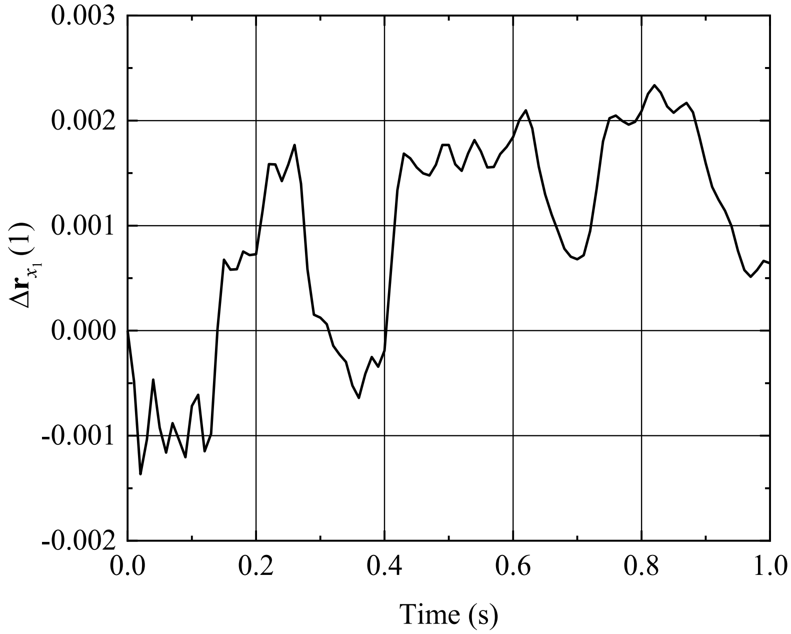

Figure 3. Gradient coordinate at point B predicted using ANCF solid element in the case of soft material without curvature constraints

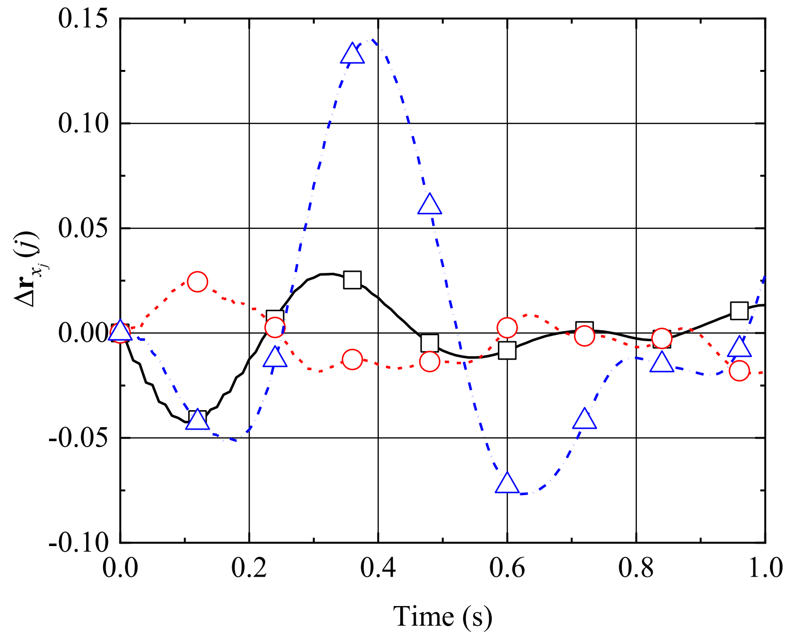

Figure 4. Difference in the gradient coordinates at point B when using ANCF tetrahedral element in the case of soft material without curvature constraints

(—□— $\Delta \mathbf{r}_{x_1}(1)$, ···○··· $\Delta \mathbf{r}_{x_2}(2)$, -·-△-·- $\Delta \mathbf{r}_{x_3}(3)$)

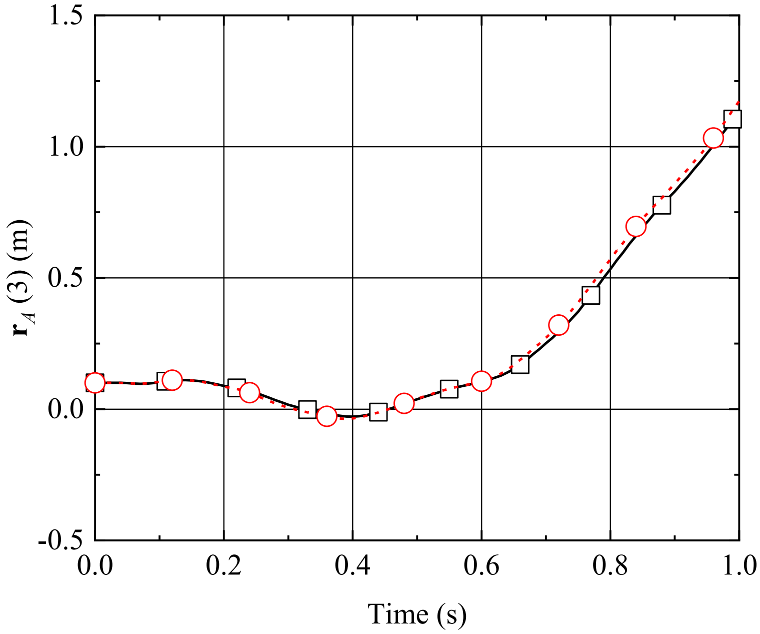

Figure 5. X_3 -displacement of tip point A using in the case of soft material predicted using ANCF solid-element mesh
(Without curvature constraints, With curvature constraints)

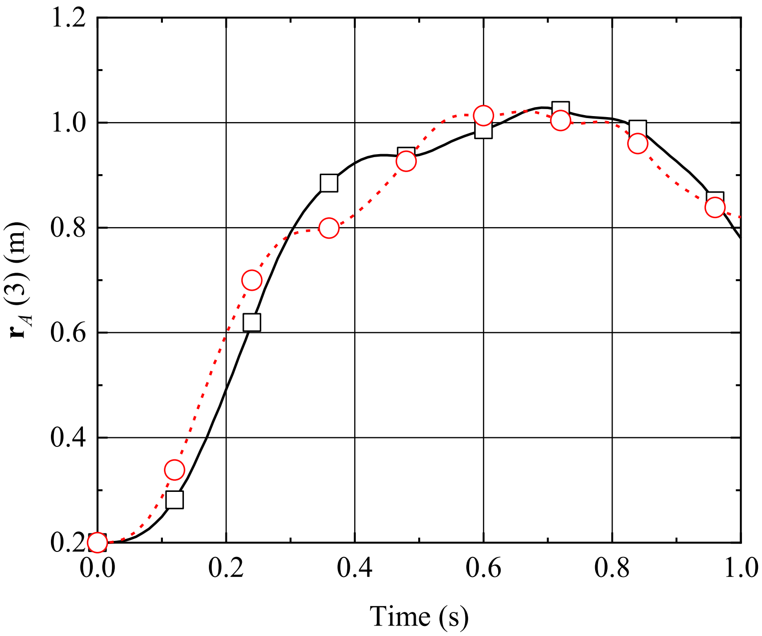

Figure 6. X_3 -displacement of tip point A in the case of soft material using ANCF tetrahedral-element mesh
(Without curvature constraints, With curvature constraints)

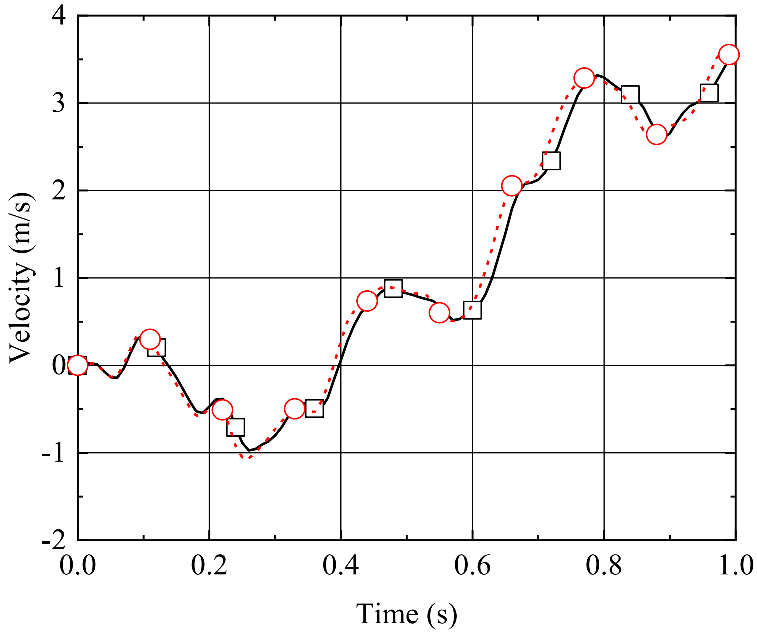

Figure 7. Velocity of tip point A using in the X_3 direction in the case of soft material predicted using ANCF solid-element mesh
(—□— Without curvature constraints, ···○··· With curvature constraints)

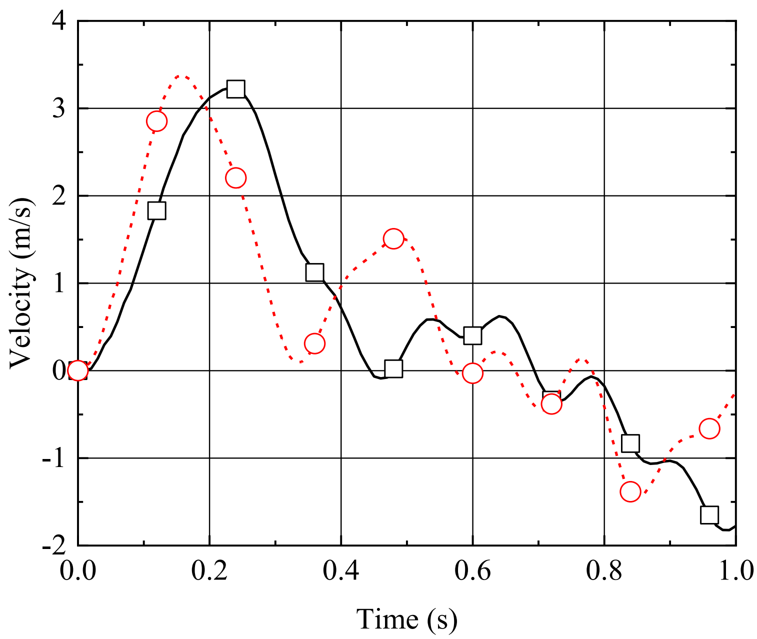

Figure 8. Velocity of tip point A using in the X_3 direction in the case of soft material predicted using ANCF tetrahedral-element mesh
(—□— Without curvature constraints, ···○··· With curvature constraints)

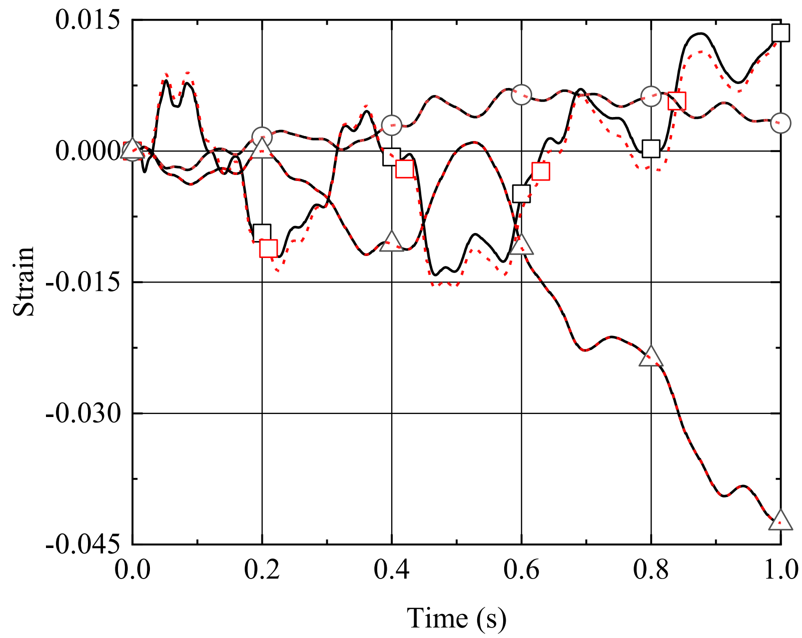

(a)

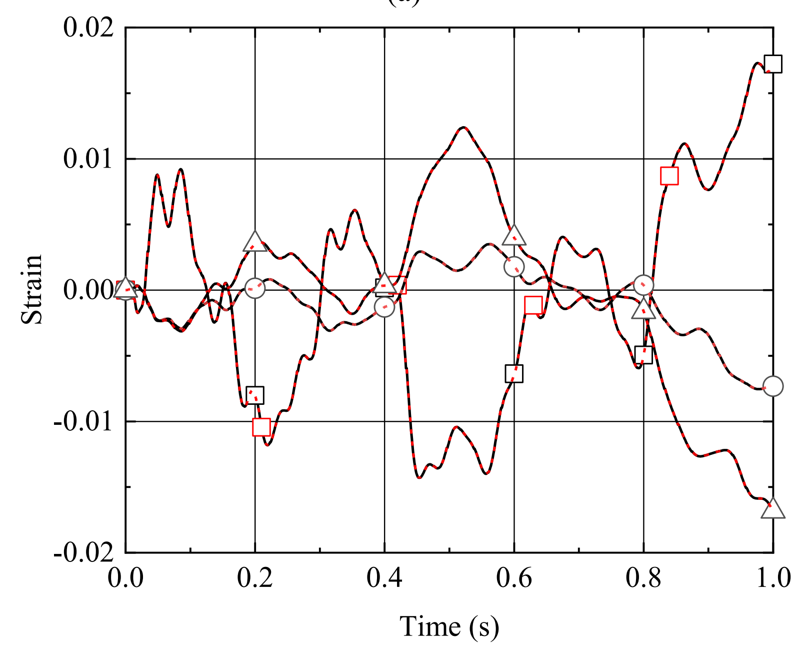

(b)

Figure 9. Normal strain change at point B when using ANCF solid element in the case of soft material

((a). Without curvature constraints, (b). With curvature constraints)

(—□— $\varepsilon_{x_1x_1}$,—○— $\varepsilon_{x_2x_2}$, —△— $\varepsilon_{x_3x_3}$), (— Element 1, - - - Element 2)

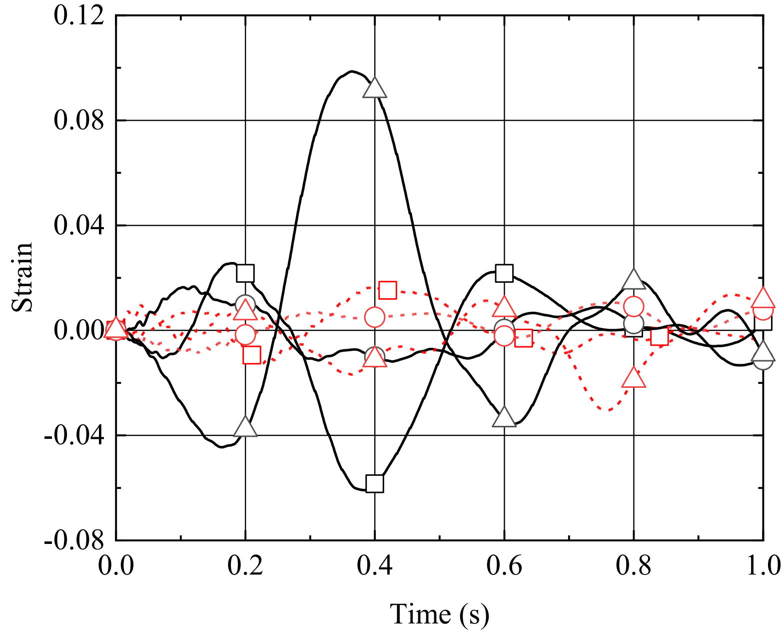

(a)

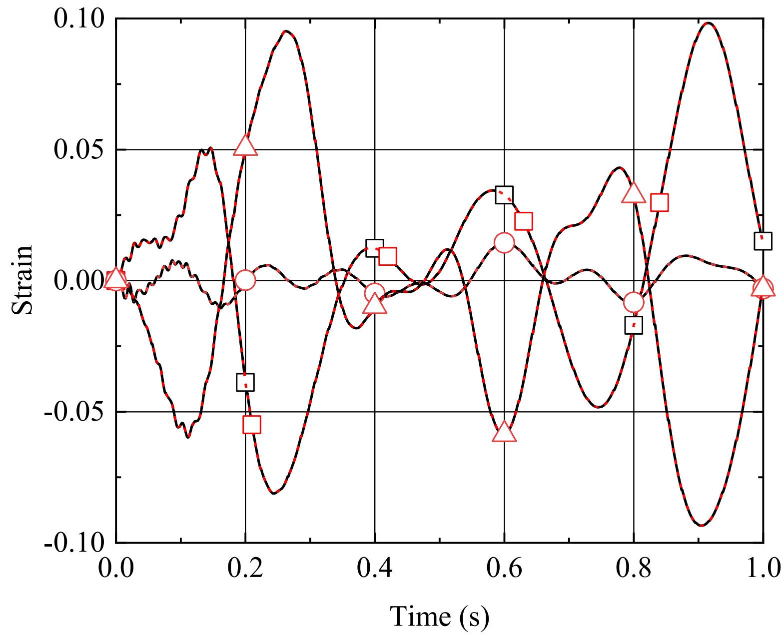

(b)

Figure 10. Normal strain change at point B when using ANCF tetrahedral element in the case of soft material

((a). Without curvature constraints, (b). With curvature constraints)

(—□— $\varepsilon_{x_1x_1}$,—○— $\varepsilon_{x_2x_2}$, —△— $\varepsilon_{x_3x_3}$), (▬ Element 1, - - - Element 2)

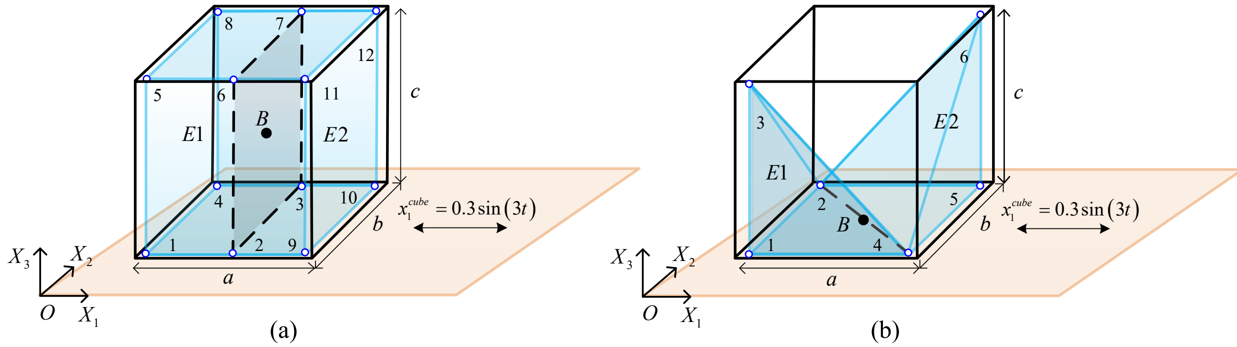

Figure 11. Fluid sloshing example
(a) ANCF solid-element mesh, (b) ANCF tetrahedral-element mesh

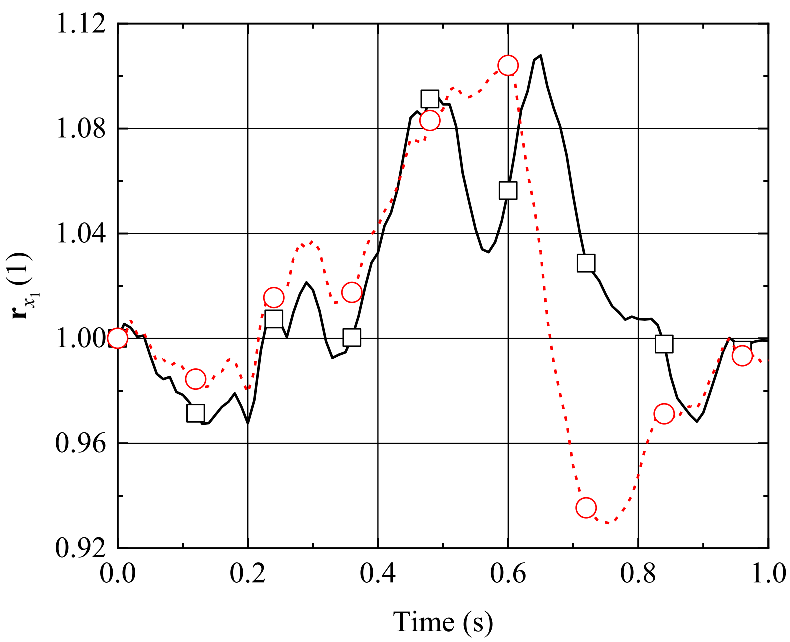

Figure 12. Gradient coordinate at point B predicted using ANCF solid element in the case of fluid material without curvature constraints
(—□— Element 1, ···○··· Element 2)

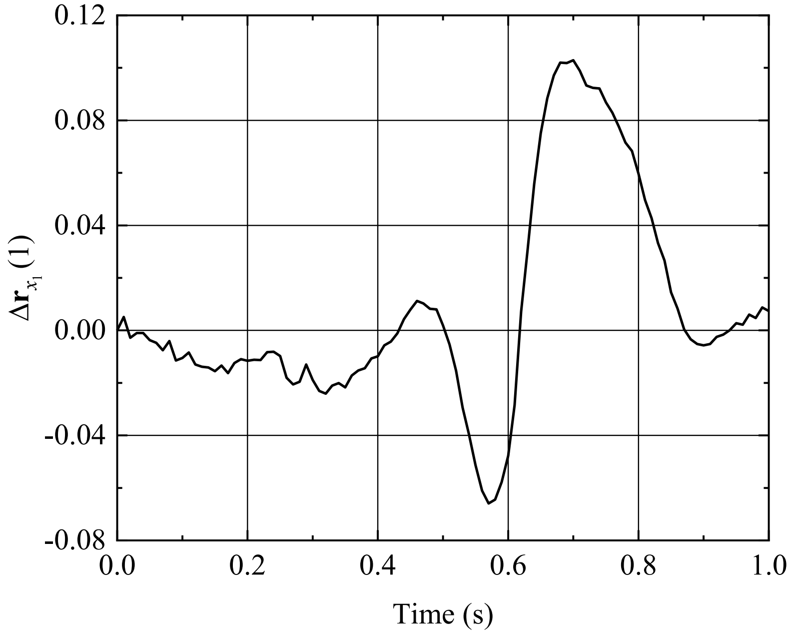

Figure 13. Difference in the gradient coordinate at point B predicted using ANCF solid element in the case of fluid material without curvature constraints

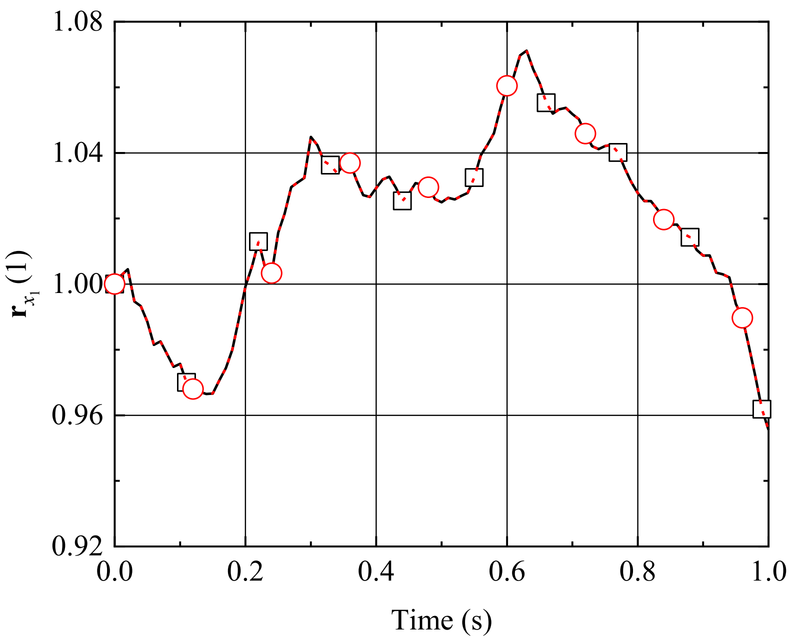

Figure 14. Gradient coordinate at point B predicted using ANCF solid element in the case of fluid material with curvature constraints
(—□— Element 1, ···○··· Element 2)

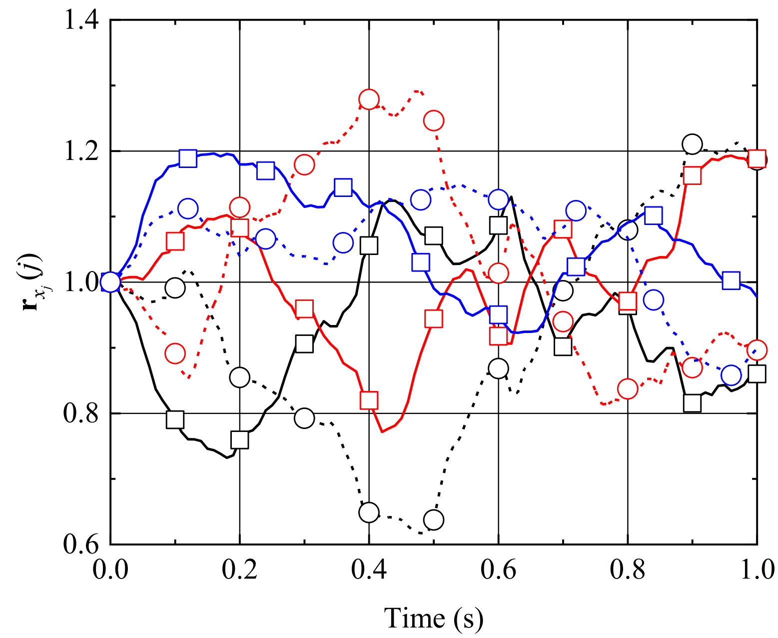

Figure 15. Gradient coordinates at point B predicted using ANCF tetrahedral element in the case of fluid material without curvature constraints

($\mathbf{r}_{x_1}(1)$, $\mathbf{r}_{x_2}(2)$, $\mathbf{r}_{x_3}(3)$), (Element 1, Element 2)

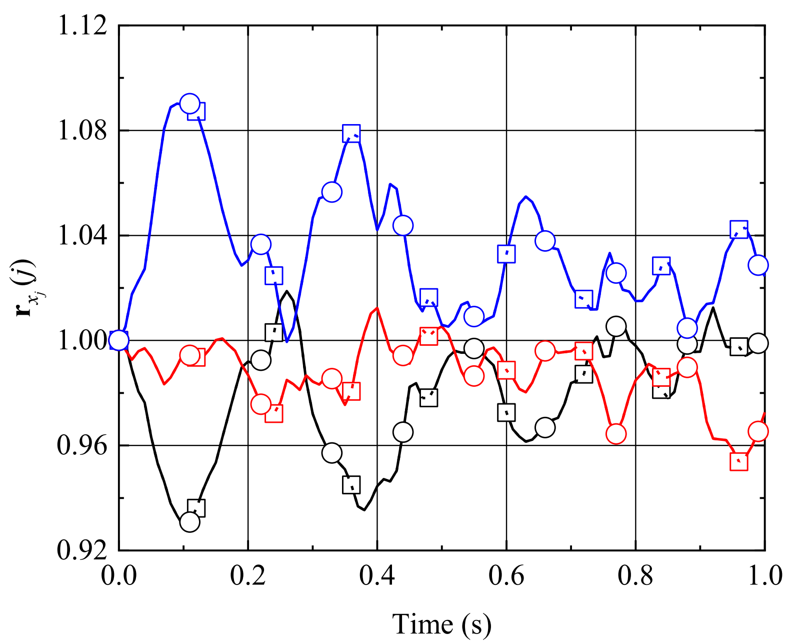

Figure 16. Gradient coordinates at point B predicted using ANCF tetrahedral element in the case of fluid material with curvature constraints

($\mathbf{r}_{x_1}(1)$, $\mathbf{r}_{x_2}(2)$, $\mathbf{r}_{x_3}(3)$), (Element 1, Element 2)

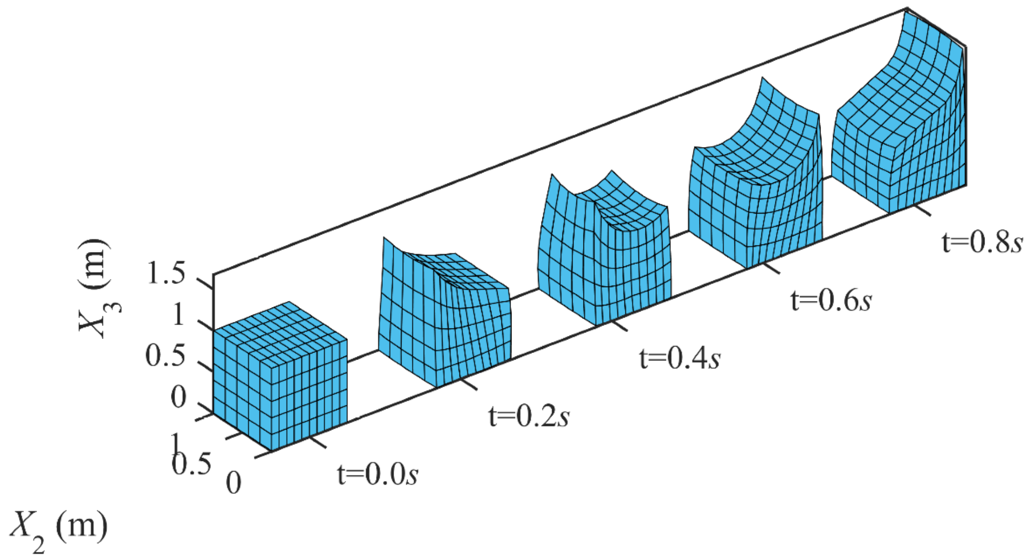

(a)

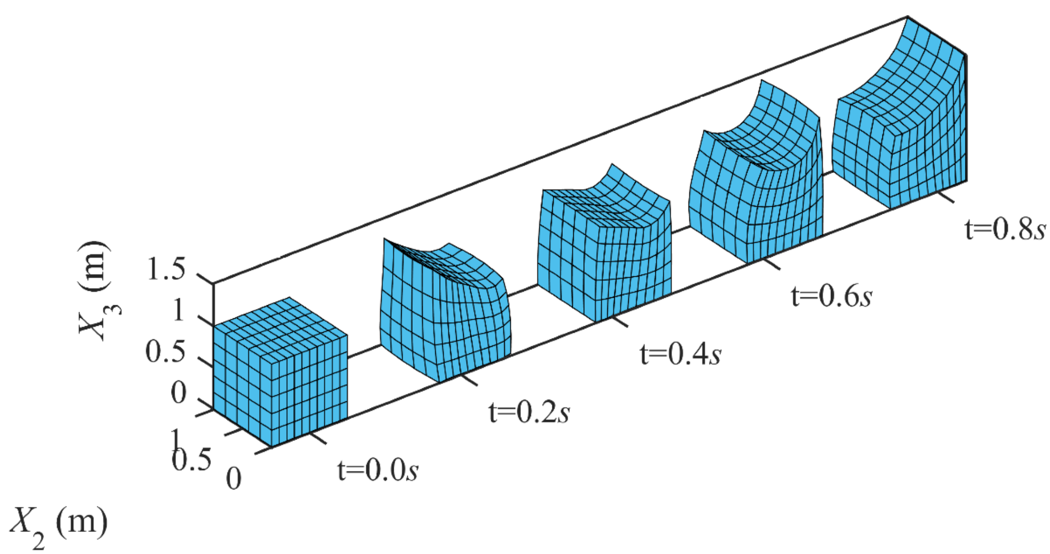

(b)

Figure 17. Fluid deformed shape using ANCF solid-element mesh
(a) Without curvature constraints, (b) With curvature constraints

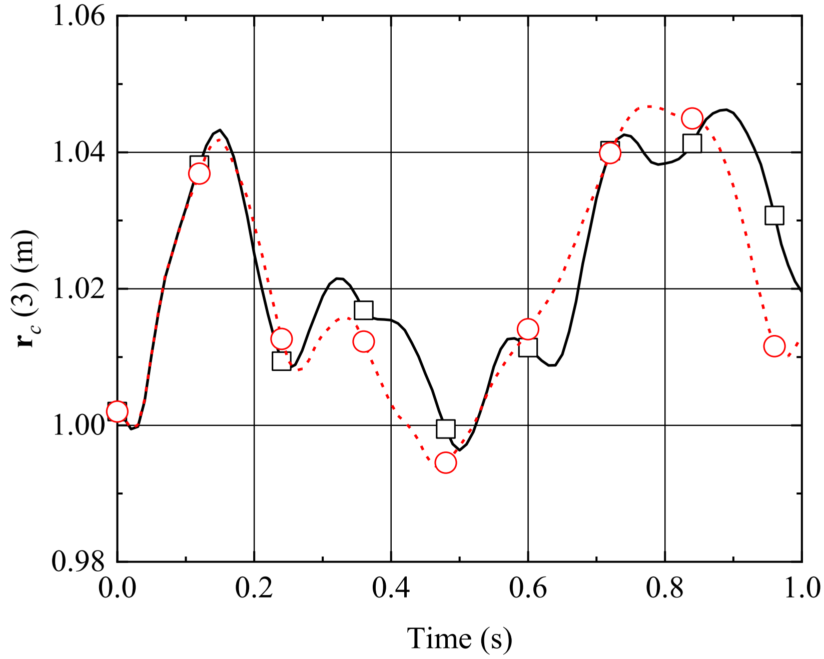

Figure 18. Mass-center X_3-displacement in the case of fluid material predicted using ANCF solid-element mesh

(—□— Without curvature constraints, ···○··· With curvature constraints)

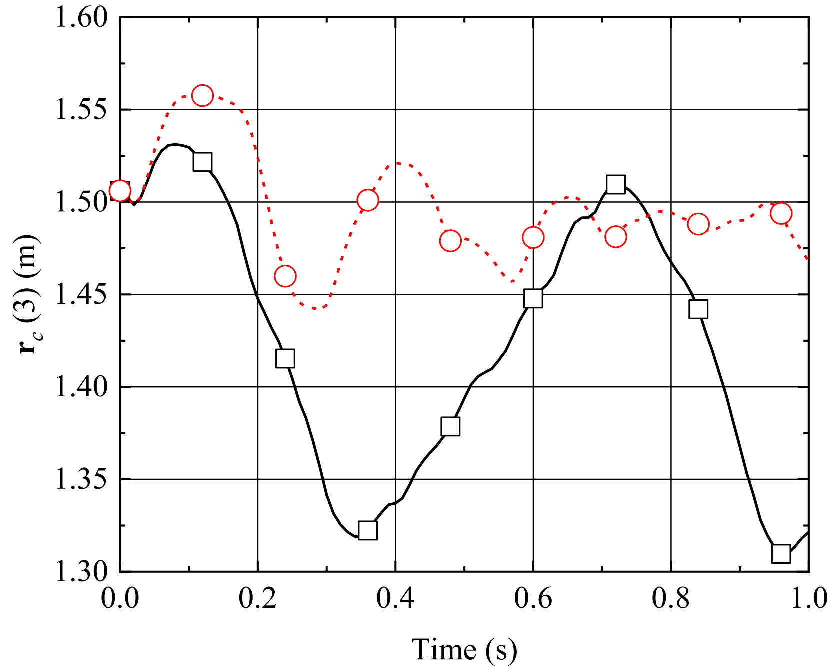

Figure 19. Mass-center X_3-displacement in the case of fluid material predicted using ANCF tetrahedral-element mesh

(—□— Without curvature constraints, ···○··· With curvature constraints)

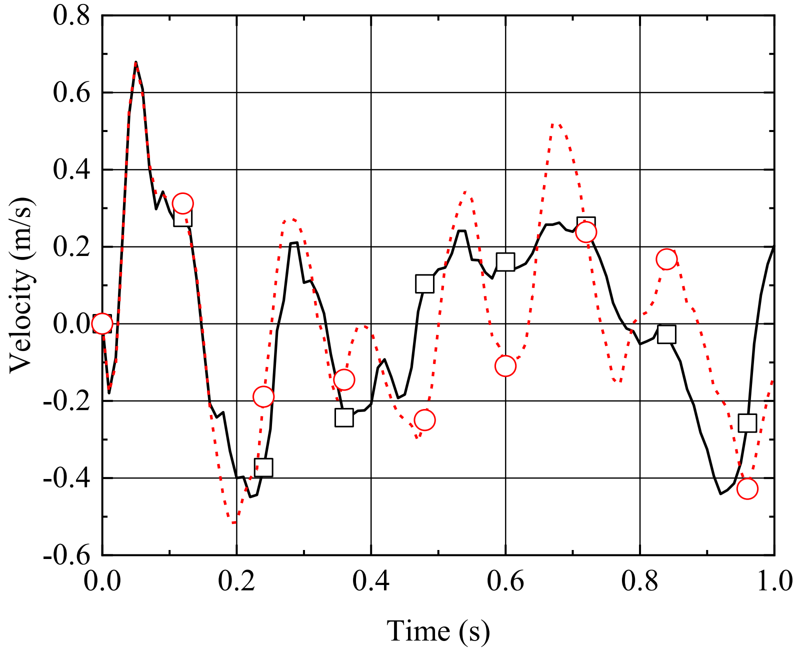

Figure 20. Mass-center X_3-velocity in the case of fluid material predicted using ANCF solid-element mesh
(—□— Without curvature constraints, ···○··· With curvature constraints)

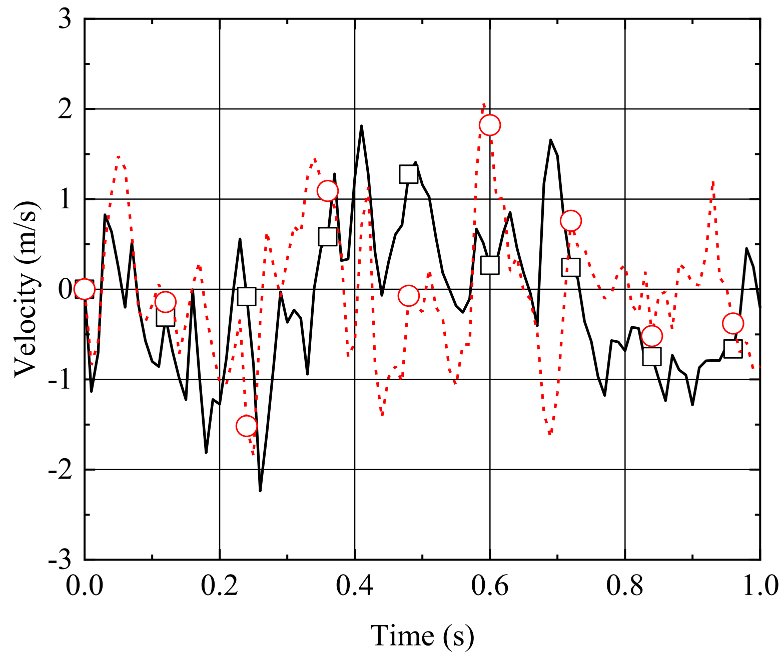

Figure 21. Mass-center X_3-velocity in the case of fluid material predicted using ANCF tetrahedral-element mesh
(—□— Without curvature constraints, ···○··· With curvature constraints)

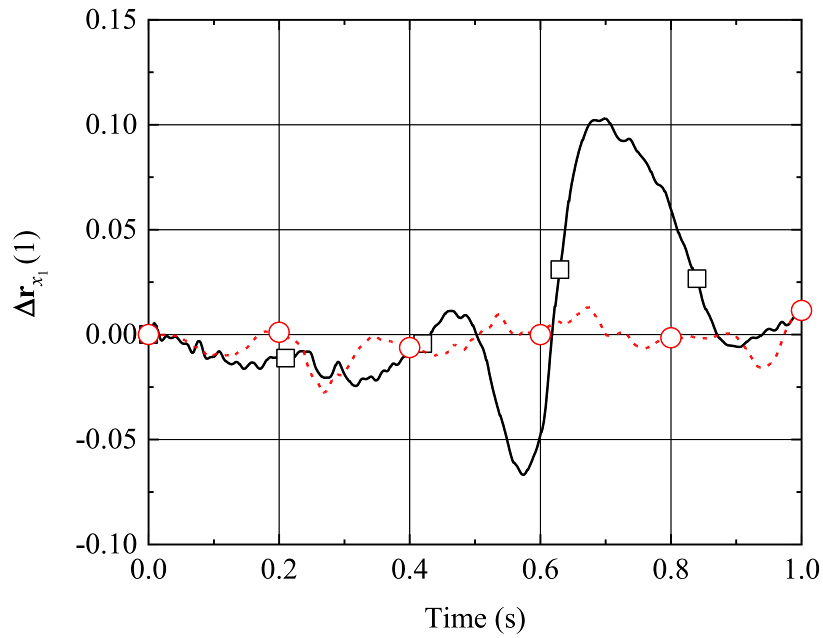

Figure 22. Influence of penalty coefficient on the gradient coordinate difference at point B when using ANCF solid element in the case of fluid material without curvature constraints ($k_{IC} = 1\times 10^{7}$, $k_{IC} = 1\times 10^{8}$)

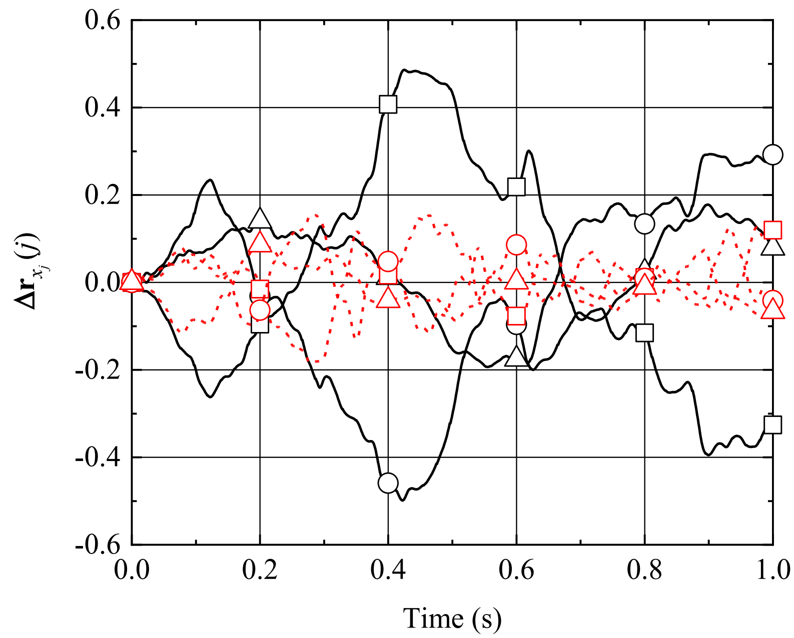

Figure 23. Influence of penalty coefficient on the gradient coordinate difference at point B when using ANCF tetrahedral element in the case of fluid material without curvature constraints ($\Delta \mathbf{r}_{x_1}(1)$, $\Delta \mathbf{r}_{x_2}(2)$, $\Delta \mathbf{r}_{x_3}(3)$), ($k_{IC} = 1\times 10^{7}$, $k_{IC} = 1\times 10^{8}$)

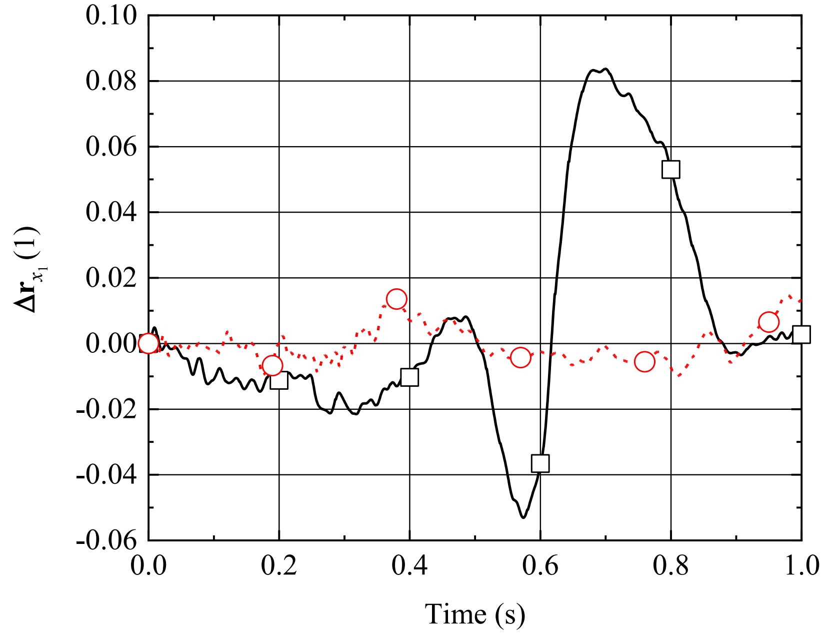

Figure 24. Influence of mesh size on the gradient coordinate difference at point C when using ANCF solid element in the case of fluid material (—□— 2 elements, ···○··· 8 elements)

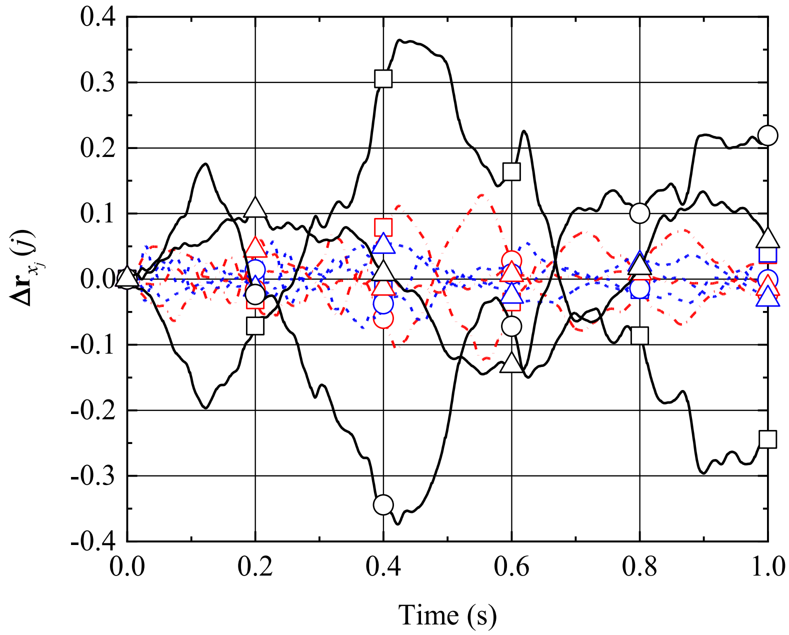

Figure 25. Influence of mesh size on the gradient coordinate difference at point D when using ANCF tetrahedral element in the case of fluid material (—□— $\Delta \mathbf{r}_{x_1}(1)$, —○— $\Delta \mathbf{r}_{x_2}(2)$, —△— $\Delta \mathbf{r}_{x_3}(3)$) (—2 elements, -·-5 elements, - - - 40 Elements)

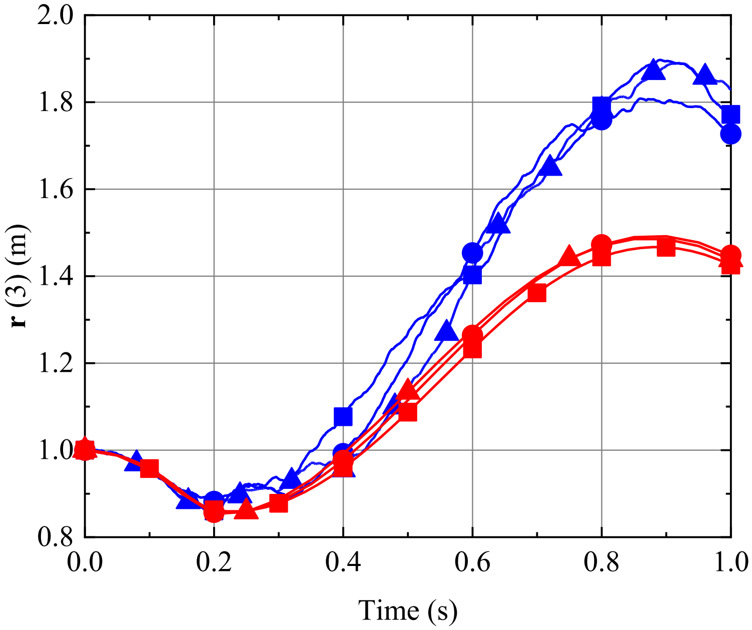

Figure 26. Comparison test in the case of ANCF solid element and LsDyna solid element (ANCF $4\times4\times4$ elements, ANCF $5\times5\times5$ elements, ANCF $6\times6\times6$ elements; Ls-Dyna $40\times40\times40$ elements, Ls-Dyna $50\times50\times50$ elements, Ls-Dyna $60\times60\times60$ elements)